Relationship between latent and radiative heating fields of Tropical cloud systems using synergistic satellite observations

Xiaoting Chen[1], Claudia J. Stubenrauch[1], and Giulio Mandorli[1]

[1]Laboratoire de Météorologie Dynamique/Institut Pierre-Simon Laplace, (LMD/IPSL), Sorbonne Université, Ecole Polytechnique, CNRS, Paris, France

Correspondence: Xiaoting Chen (xiaoting.chen@lmd.ipsl.fr)

Abstract. In order to investigate the relationship between latent and radiative heating (LH, RH), particularly within mesoscale convective systems (MCSs), we used synergistic satellite-derived data from active instruments. Given the sparse sampling of these observations, we expanded the Spectral LH profiles derived from the Tropical Rain Measurement Mission (TRMM–SLH) by applying artificial neural network regressions on Clouds from InfraRed Sounder data and meteorological reanalyses, following a similar approach as for the expansion of the RH profiles. The zonal averages of vertically integrated LH (LP) at 1:30 AM and PM LT align well with those from the full diurnal sampling of TRMM–SLH over ocean. For Upper Tropospheric (UT) clouds releasing large latent heat, the surface temperature has a larger impact on the atmospheric cloud radiative effect (ACRE) in dry than in humid environments, while for lower clouds, producing relatively small latent heat, humidity plays a large role in enhanced ACRE. The distribution of UT clouds in the LP–ACRE plane shows a very large spread in ACRE for small LP, which is gradually reduced towards larger LP. The mean ACRE per MCS increases with LP, ranging from 50 to 115 W m^{-2}. As expected, the shapes of the LH profiles of mature MCSs show that larger, more organized MCSs have a larger contribution of stratiform rain than the smaller MCSs. Convective organization enhances the mean ACRE of the MCS by up to 20 W m^{-2}.

1   Introduction

Clouds envelop approximately two-thirds of the Earth's surface, with 40 % originating from upper tropospheric (UT) clouds (e.g., Stubenrauch et al., 2013, 2017). These cloud formations play a crucial role in modulating the Earth's energy budget and heat transport. They are most abundant in the tropics, constitute around 60 % of the total tropical cloud distribution and often form as cirrus anvils from convective outflow, building mesoscale convective systems (MCS), as illustrated by Houze (2004). Latent heat is released into the atmosphere by the precipitating parts of these MCSs.

Throughout the precipitation process, latent heating (LH) is generated within the convective cores and denser regions of the anvils due to the condensation process, which involves the phase transition of water vapor into tiny liquid or frozen cloud particles. The release of latent heat strongly influences the atmospheric circulation, particularly in the tropics (Tao et al., 2006). Therefore, the interpretation of latent heat release and its fluctuations plays a central role in the complex interactions of the Earth's water and energy cycles (e.g., Gill, 1980; Mapes, 1993; Schumacher et al., 2004; Tao et al., 2016). Radiative heating (RH) of UT clouds further augments this energy reservoir by at least 20 % (Bergman and Hendon, 2000; Li et al., 2013;

25 Stubenrauch et al., 2021). Given the significance of both processes, this article aims to study closer the relationship between latent and radiative heating, comparing different environments with a focus on MCS.

In order to study the relationship between latent and radiative heating, we have combined information from multiple satellite instruments. The heating profiles are obtained from active measurements which only overlap over a small portion in space and in time with the cloud top properties from passive remote sensing. Previously, we have expanded this vertical information by

30 using machine learning (ML) techniques (Stubenrauch et al., 2021), leading to 3D fields of radiative heating at specific local times (LTs). This article describes the expansion of the latent heating and shows to what extent these 3D latent heating fields at specific LTs represent the daily mean tropical latent heating. In addition, a cloud system approach (Stubenrauch et al., 2023) is used to identify MCSs and to determine their size, which is related to convective organization (e.g., Houze and Hobbs, 1982; Moncrieff, 1992).

35 Infrared sounders, with their good spectral resolution, are sensitive to cirrus during both day and night (e.g., Wylie et al., 2005; Stubenrauch et al., 2006, 2017, 2024). For this reason, we use cloud top properties retrieved from measurements of the Atmospheric Infrared Sounder (AIRS) onboard the National Aeronautics and Space Administration (NASA) Earth Observation Satellite Aqua and of the Infrared Atmospheric Sounding Interferometer (IASI) onboard the EUMETSAT Meteorological Operation satellite (Metop). These instruments are along-track scanners with wide swaths, with a horizontal coverage of about

40 70 % at a specific local time in the tropics.

Active sensors, the CALIPSO (Cloud-Aerosol Lidar and Infrared Pathfinder Satellite Observation) lidar and the CloudSat radar, are part of the A-Train satellite constellation (Stephens et al., 2018) and work in synergy with Aqua since 2006. They provide observations of the vertical structure of clouds (e.g., Mace et al., 2009), radiative heating rates (Henderson et al., 2013), as well as information on precipitation (Haynes et al., 2009). However, these parameters are only available along successive

45 narrow nadir tracks (~2500 km apart).

The satellite orbit of the Tropical Rainfall Measuring Mission (TRMM) allowed to statistically sample the full diurnal cycle (Negri et al., 2002). Latent heating profiles have been estimated from the Precipitation Radar (PR) onboard TRMM via the Spectral Latent Heating (SLH) algorithm (Shige et al., 2004). However, within a time window of about one hour, the TRMM data only cover a very small fraction of the tropics of approximately 7 %. For the expansion towards 3D latent heating fields at

50 the specific LTs of AIRS (1:30 AM / PM) and IASI (9:30 AM / PM), we have used a similar approach as in Stubenrauch et al. (2021). While CALIPSO–CloudSat only overlap with AIRS observations, TRMM observations overlap with both, AIRS and IASI observations.

Sections 2.1 to 2.3 first present the data: latent heating profiles from TRMM PR measurements, cloud properties from AIRS and IASI, 3D structure and precipitation intensity classification from machine learning trained on CloudSat–CALIPSO.

55 Sections 2.4 and 2.5 describe their collocation as well as the training and evaluation of the artificial neural networks (ANN) to expand the TRMM–SLH heating profiles. Section 3 outlines the construction of the 3D LH dataset, over the period 2004–2018, and shows its coherence in comparison to the original TRMM data. Section 4 describes the reconstruction of the MCSs using the CIRS data. Section 5 discusses the results on the relationship between latent and radiative heating, while Section 6 summarizes the key conclusions and suggests future research directions.

60   In our analyses, we use the following definitions: LH for latent heating profile, LP for vertically integrated LH, RH for radiative heating profile, CRE for cloud radiative effect on the radiative heating profile, ACRE (atmospheric cloud radiative effect) for the vertically integrated CRE.

2   Data, Methods and Evaluation

2.1   Latent heating data

65   The primary objective of the TRMM mission (Houze Jr. et al., 2015; Kummerow et al., 1998; Liu et al., 2012; Dorian, 2014) was to study the temporal and spatial variability of tropical rainfall. For this purpose, TRMM has an orbital inclination at 35° with 16 orbits per day. TRMM revisits a given area at the same LT every 23 (near equator) to 46 days (near 35°) (Negri et al., 2002). Therefore, TRMM–PR estimates over any one hour, even with 3 years of data, are insufficient to accurately describe the diurnal cycle of precipitation for grid sizes smaller than 12°, due to inconsistent spatial sampling. The PR is a radar operating at

70   the K_u-band in the microwave range around 13.8 GHz, specifically dedicated to obtain the vertical profiles of precipitation, with a horizontal resolution of about 5 km and a swath width of 247 km. The radar measures the precipitation top height, melting layer as well as the rain intensity vertical structure and distinguishes convective and stratiform rain. The TRMM mission took data from 1997 until 2015 and was then continued by the Global Precipitation Measurement Mission (GPM).

The TRMM mission employs two recognized retrieval algorithms for LH estimates (Tao et al., 2022): the Convective-

75   Stratiform Heating (CSH, Tao et al., 2018) and the Spectral Latent Heating (SLH, Shige et al., 2004). Both retrievals explicitly use look up tables (LUT) which include LH profiles simulated by cloud-resolving models (CRMs) as function of precipitation rate and other parameters.

In the CSH algorithm, diabatic heating is calculated based on the surface rainfall rate and its associated stratiform fraction derived from the PR. The CSH algorithm utilizes a LUT containing rain-normalized heating profiles, categorized into three

80   convective and stratiform rain types (oceanic, continental, and shallow), representing different cloud systems across diverse geographical locations. The profiles are produced through CRM simulations validated against sounding observations in specific tropical regions. The heating depth varies based on the PR echo-top height, with its magnitude determined by the PR surface precipitation amount (Hagos et al., 2010).

The SLH algorithm (Shige et al., 2004, 2007, 2008) follows a similar approach as the CSH algorithm, with the key difference

85   being continuous vertical profiles of latent heating simulated as function of the PR echo-top height. Deep stratiform rain is subdivided into two categories: one with decreasing precipitation from the melting level to the surface and another with increasing precipitation from the melting level to the surface (Shige et al., 2013). The level of maximum diabatic heating from SLH is higher relative to CSH, as shown by Elsaesser et al. (2022). This difference can arise from the utilization of distinct CRM-simulated heating profiles to generate the LUTs. Firstly, shallow convective heating is more explicitly retrieved

90   by the SLH algorithm, as it uses observed information on precipitation top height. However, the SLH product is developed using diabatic heating data from the Tropical Ocean Global Atmosphere-Coupled Ocean-Atmosphere Response Experiment (TOGA COARE) field campaign simulations, while the LUTs for the CSH product utilize various tropical land and ocean

field campaign simulations. It is noteworthy that TOGA COARE convection is characterized by larger fractions of stratiform precipitation (Tao et al., 2016). Nevertheless, SLH agrees better with reanalysis estimates and provides more detailed low-level heating information (Hagos et al., 2010; Tao et al., 2022).

In this investigation, we utilize the latent heating profiles of the GPM TRMM SLH dataset (V06, Shige et al., 2009), given at specific local observation times, at a spatial resolution of $0.5° \times 0.5°$ and a vertical resolution of 250 m. We used the unconditional mean LH profiles, computed from all measurements within each grid cell.

2.2 Cloud and atmospheric data

The AIRS instrument (Chahine et al., 2006) aboard the polar-orbiting satellite Aqua offers high spectral resolution measurements of the Earth's atmosphere at 1:30 AM and 1:30 PM LT since 2002. Its spectral coverage spans 2378 radiance channels within the wavelength range of 3.7–15.4 μm (650–2700 cm^{-1}). AIRS footprints are grouped as a 3×3 arrays. The spatial resolution of an AIRS footprint is about 13.5 km at nadir, and the swath width is approximately 1650 km. The latter leads to a substantial coverage of approximately 70 % at a specific local time in the tropics.

The IASI instruments (Hilton et al., 2012) are operational on the European Metop platforms, starting data acquisition in 2007. They provide measurements at 9:30 AM and 9:30 PM LT. IASI is a hyperspectral and high-precision Fourier transform spectrometer developed in collaboration by CNES (Centre National d'Etudes Spatiales) and EUMETSAT. It covers the infrared spectral domain from 3.6 to 15.5 μm and offers data across 8461 spectral channels. Employing a cross-track scanning mechanism, the swath comprises 30 effective fields per scan, each consisting of a 2×2 array of footprints (August et al., 2012). The spatial resolution of an IASI footprint is about 12 km at nadir, and the swath width is about 2200 km, leading to a 77 % coverage at a specific local time in the tropics.

The Clouds from IR Sounders (CIRS) retrieval reconstructs cloud properties from both AIRS and IASI measurements. It relies on a weighted χ^2 methodology employing 8 channels in the vicinity of the 15 μm CO_2 absorption band as explained by Stubenrauch et al. (2009, 2017). This retrieval simultaneously provides cloud emissivity (ϵ_{cld}) and pressure (P_{cld}), along with associated uncertainties. The retrieval has been applied to both AIRS and IASI measurements. The choice of 8 channels was made to establish a consistent long-term cloud climatology by employing the same retrieval method across AIRS, IASI, and High-Resolution Infrared Radiation Sounder (HIRS) data (Stubenrauch et al., 2006). CIRS cloud types are defined according to P_{cld} and ϵ_{cld} as high clouds ($P_{cld} < 440$ hPa), which are further categorized into high opaque clouds (Cb) with $\epsilon_{cld} > 0.95$, cirrus clouds (Ci) with $0.95 > \epsilon_{cld} > 0.5$, and thin cirrus (thin Ci) clouds with $0.5 > \epsilon_{cld} > 0.05$, mid-level clouds (440 hPa < $P_{cld} < 680$ hPa) and low-level clouds ($P_{cld} > 680$ hPa). The latter two are further divided into opaque clouds with $\epsilon_{cld} > 0.5$ and partly cloudy with $\epsilon_{cld} < 0.5$.

For a consistent diurnal cloud variability from AIRS and IASI (Feofilov and Stubenrauch, 2019), the CIRS cloud retrieval uses auxiliary data (surface pressure and temperature, atmospheric temperature and humidity profiles, snow and sea ice information) from an identical source: ERA-Interim, obtained from the European Centre for Medium-Range Weather Forecasts (ECMWF) meteorological reanalysis (Dee et al., 2011). These atmospheric profiles are also used to convert cloud pressure to cloud temperature (T_{cld}) and cloud height (Z_{cld}).

The ERA-Interim reanalyses have a spatial resolution of $0.75° \times 0.75°$ and are available at 00:00, 06:00, 12:00, and 18:00 UTC. They have been interpolated to AIRS and IASI observation times by employing a cubic spline function.

2.3 Input data for the artificial neural networks

130   Table 1 summarizes the input variables which are used in the artificial neural network predictions described in section 2.5.1.

Since the target data are given at a spatial resolution of $0.5°$, we adapt the input data by gridding them also to $0.5°$. Atmospheric properties (specific humidity and temperature profiles within 10 layers, total precipitable water, tropopause height) and surface properties (pressure and temperature) are averaged over $0.5°$, as well as cloud properties such as P_{cld} and ϵ_{cld} and their uncertainties. In addition, we keep the cloud properties averaged over the most frequent scene (UT or mid- and low-level

135   clouds) in each grid cell. We also utilize the sub-grid structure within the grid cells: fractions of Cb, Ci, thin Ci, mid- / low-level clouds, and clear sky. The spectral variability of the effective cloud emissivity between 9 and 12 μm, computed by using the retrieved P_{cld}, indicates if the footprint is partly cloudy (Stubenrauch et al., 2017). Additional variables are the atmospheric window IR brightness temperature and its spatial variability, brightness temperature differences between atmospheric window and water vapour absorption channels, and the number of atmospheric layers down to surface.

140   Furthermore, we have used several variables for a scene identification, but they are not considered as input variables: Cloud top height (Z_{top}), normalized cloud vertical extent (difference between cloud top and cloud base and divided by cloud top, represented as DZnorm = (Z_{top}-Z_{base})/Z_{top}), fraction of clouds below the clouds identified by CIRS. These variables have been obtained by artificial neural network (ANN) regression, trained with CloudSat–CALIPSO layer information. The rain intensity classification (no rain, light rain, heavy rain), determined by ANN trained with precipitation data from CloudSat,

145   considers light rain to be < 5 mm h^{-1} and heavy rain > 5 mm h^{-1} (Stubenrauch et al., 2023).

Table 1. List of input variables for the prediction of latent heating: gridded over $0.5° \times 0.5°$

Input variables	Definitions
Clouds	
$\epsilon_{\text{cld}}, P_{\text{cld}}, T_{\text{cld}}, Z_{\text{cld}}, d\epsilon_{\text{cld}}, dP_{\text{cld}}$	CIRS cloud properties and uncertainties
$\epsilon(\text{scene}), P(\text{scene}), \text{frac\_scene}$	CIRS cloud properties and fraction of most frequent scene
$\sigma(\epsilon(\lambda_i)))$	Spectral variability of effective cloud emissivity over six wavelengths (9-12 μm)
Atmosphere	
$\text{TB}(11.85\mu m), \sigma(\text{TB})$	AIRS / IASI brightness temperatures and spatial variability
$\text{TB}(11.85\mu m) - \text{TB}(7.18\mu m), \text{TB}(11.85\mu m) - \text{TB}(7.23\mu m)$	Brightness temperature difference between atmospheric window and water vapour absorption channels
q, T within 10 layers	ERA-Interim specific humidity and temperature profile
total precipitable water, $P_{\text{tropopause}}$	ERA-Interim column water vapour, tropopause height
Surface	
$P_{\text{surf}}, T_{\text{surf}}, \text{nb of atm. layers down to } P_{\text{surf}}$	ERA-Interim surface properties
Sub-grid structure of CIRS cloud types from footprints	
$\text{frac\_Cb}, \text{frac\_Ci}, \text{frac\_thCi}$	Fraction of cumulonimbus, cirrus, thin cirrus
frac_mlow	Fraction of mid and low level clouds
frac_clr	Fraction of clear sky

*scene: 1 for high level clouds and 2 for mid-low level clouds.

2.4 Collocation of input and target data

Due to their different orbit characteristics, the observations from the TRMM, Aqua and Metop satellites seldom coincide in both time and geographical location when observing the Earth. Consequently, only a subset of their respective observational databases can be overlaid and employed for the training. We allow a 20-minute time differential between the CIRS and TRMM data. AIRS orbits (1:30 AM and 1:30 PM) and IASI orbits (9:30 AM and 9:30 PM LT) are independently co-located with TRMM orbits. Figure 1 illustrates the different swath width of the Aqua–AIRS and TRMM–PR measurements and their coincidence for a specific day at a specific observation time. Within a time window of ±20 minutes, the overlap between the TRMM-PR and the AIRS measurements is only 3 %. We expand this coverage to about 70 % and 77 % (swath coverage of AIRS and IASI, respectively) by applying ANN methods to the input data described in section 2.3. This allows us then to relate horizontal fields of clouds, LH and RH at specific local times, as shown in section 3.

The co-located AIRS–TRMM data spanning from 2004 to 2013 and IASI–TRMM data from 2008 to 2014 correspond to about 300000 cases, for each of the four measurement times.
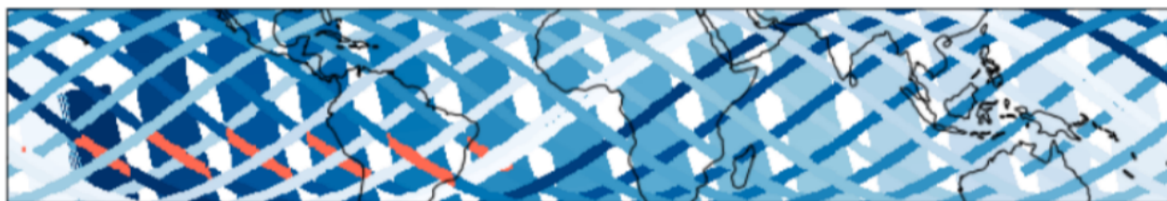
Figure 1. Illustration of the temporal and spatial match between Aqua–AIRS and TRMM–PR orbits. Orange represents the satellite trace segments where the data can be jointly acquired by Aqua and TRMM at 1:30 AM LT, within a time window of ± 20 minutes, for one specific day.

2.5 Artificial Neural Network predictions and evaluation

2.5.1 Development of prediction models

160 As the distribution of precipitation rates is very skewed, with a maximum at 0 mm h^{-1} and a very long tail towards larger values, we first examine the shapes and statistics of the TRMM–SLH latent heating profiles within the collocated data. These can be categorized by rain intensity (Fig. 2) or by normalized vertical cloud extent (Fig. S1). In general, convective towers which produce a strong latent heating can be identified by a heavy rain rate or by a large vertical extent. However, these occur much less frequently (10 %) than scenes of lightly precipitating (25 %) and non-precipitating (65 %) UT clouds. Over land the

165 diurnal variation of these convective towers is larger than over ocean, as expected, with a minimum in the morning (7 %) and a maximum in the evening (12 %), while non-precipitating UT clouds vary from 65 % at night to 77 % in the afternoon.

Figure 2 presents LH profiles of UT clouds, separately over these three rain intensity scenes and over ocean and land, at the four CIRS observation times. This rain intensity categorization shows consistent outcomes for both ocean and land cases. As expected, the LH profiles of these three scene types differ considerably, with nearly no LH for no rain and very large LH for

170 heavy rain. The latter show large peaks in LH around 450 hPa, with a larger maximum over ocean (30 K day^{-1}) than over land (approximately 20 K day^{-1}). This may be linked to smaller systems over land than over ocean (e.g., Liu, 2007). A larger diurnal variation over land is also observed, as expected. It is interesting to note that the LH profiles categorized by normalized cloud vertical extent show a similar behaviour, as shown in Fig. S1. The very small LH peak of less than 1 K day^{-1} at about 900 hPa for non-precipitating UT clouds can be explained by lower clouds underneath which produce rain (Fig. S2). Over land,

175 this lower small peak is vertically more extended and only observed at 13:30 LT. This may be due to developing convection, which has its peak in the late afternoon, and is missed by the AIRS and IASI observation times (see section 3).

Since the LH profile shapes and statistics of the different rain intensity categories are very different, we developed ANN models for each of the three classes in rain intensity, separately over ocean and over land. For each of these precipitation classes, we also separated scenes of UT clouds and of mid- and low-level clouds. The latter show a peak of only 4 K day^{-1} at

180 about 900 hPa in the case of heavy rain (Fig. S3). This leads us to develop 12 ANN regression models to predict LH profiles from AIRS or from IASI, respectively. The predicted LH rates are given at a spatial resolution of 0.5°.
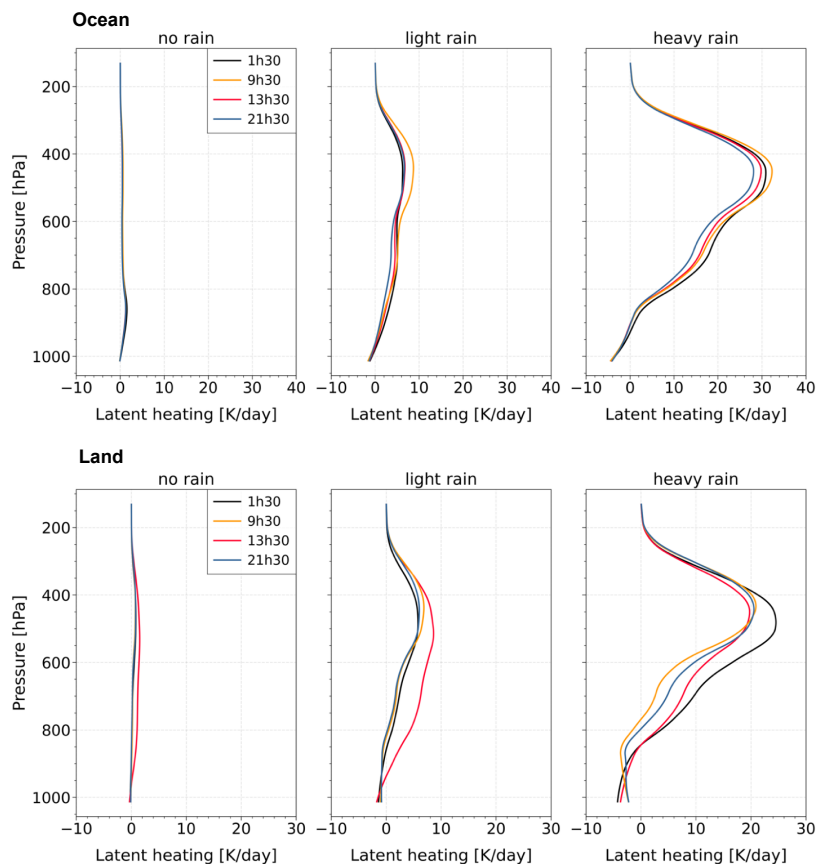
Figure 2. LH profiles of UT clouds categorized by rain intensity (no rain, light rain and heavy rain), at 4 observation times (1h30, 9h30 AM/PM), over ocean (top panels) and over land (bottom panels), from the TRMM–SLH retrieval (Shige et al., 2004, 2007, 2008) averaged over the TRMM–CIRS collocated data during the period 2008–2013, within 30°N–30°S, at a spatial resolution of 0.5°.

For the regression models, the final ANNs consist of 2 hidden layers both with 32 neurons and one output layer. We applied the Rectified Linear Unit (ReLU) activation function on the hidden layers. In addition, we used the Root Mean Square Propagation (RMSprop) optimizer with a learning rate of 0.0001 and a batch size of 512. Furthermore, we applied a Min-Max Normalization to the variables. The collocated dataset was randomly divided into three categories: 60 % for training, 20 % for validation, and 20 % for test. The latter two have not been used in the training: While the validation data are used in the iteration process, the test data are used for evaluation (section 2.5.2).

We use the Mean Squared Error (MSE) as a loss function for the regression models, which evaluates the mean squared difference between observed and predicted values. The model parameters are fitted by minimizing this loss function. The Mean Absolute Error (MAE) is the average of absolute differences between observed and predicted values, and it is used to assess the quality of these regression models. In order to avoid overfitting, we stop training when the loss function does not

improve for 20 iterations. We compare the behaviour of the loss function of the training data with the one of the validation data. Similar results suggest that the model performs consistently well on both datasets, showing a certain level of generalization ability. Figure S4 shows a good performance, except for a slight overfitting for heavy precipitation.

195   The hyper-parameter selection of the neural network may influence the training results. Therefore, we tested different deep learning parameters (e.g., number of neurons per layer, number of layers, learning rate, regression kernel) to optimize these ANN regression models. The results show only slight differences in training/validation loss and MAEs among these tests, and there was no significant impact on the LH results.

To study the impact of the variable selection on the predictions, we have experimented with various input variables, in

200   particular we included and excluded information on the rain intensity substructure within the grid boxes of 0.5°. By using this information, the results were slightly better, in particular the spread of the predicted LH was slightly larger. However, this approach resulted in a slight positive anomaly in vertically integrated LH for March 2014 and later on, when considering the timeseries of LH derived from AIRS data (not shown). The LH time series derived from IASI were not affected. In March 2014, the AIRS instrument suffered from a solar flare event which led to tiny artifacts which show in the ANN rain rate classification

205   (Stubenrauch et al., 2023). Consequently, we have excluded these grid fractions of different rain intensity classes from our input variables.

We also assessed the effectiveness of the fraction of clouds below CIRS clouds. It effectively classifies low clouds underneath (Fig. S2), but as additional input, it did not improve the results.

Therefore, we kept the configuration which uses the 27 variables given in Table 1 as input variables. For both AIRS and

210   IASI, the MAE values, presented in Table S1, are notably small. Moreover, the loss function, presented in Fig. S4, decreases rapidly with the iterations (epochs), followed by stabilization.

2.5.2   Evaluation using collocated data

We have evaluated the LH prediction results by comparing them with the original TRMM LH, using test data. Upper panels of Fig. 3 and S3 show specific patterns for the case of UT clouds. In all cases, the real data reveal a large variability between 600

215   and 800 hPa, which may be linked to the variability between stratiform and convective rain within the 0.5°.

(1) For the heavy rain case, UT clouds produce a noticeable 25 K day^{-1}LH at about 450 hPa.

(2)In the light rain case, the predicted LH exhibits a much flatter distribution with only a very small peak, of about 5 K day^{-1}at around 450 hPa.

(3) In the no-rain case, LH is close to 0 K day^{-1}, with a tiny peak of approximately 0.7 K day^{-1}in the low-altitude region

220   (P > 800 hPa), corresponding to low-level clouds, mostly underneath non-precipitating cirrus, as suggested by Fig. S2, which shows a twice as large peak when only selecting cases with clouds below according a classification from CIRS–ML (see section 2.5.1).

While the averages of the predicted results of the different scenes agree well with those of the true data, the spread of the predicted values is much smaller. This indicates that the prediction is only slightly better than a simple mean per class, because

225   the input information is not sufficient and the spatial resolution too coarse.
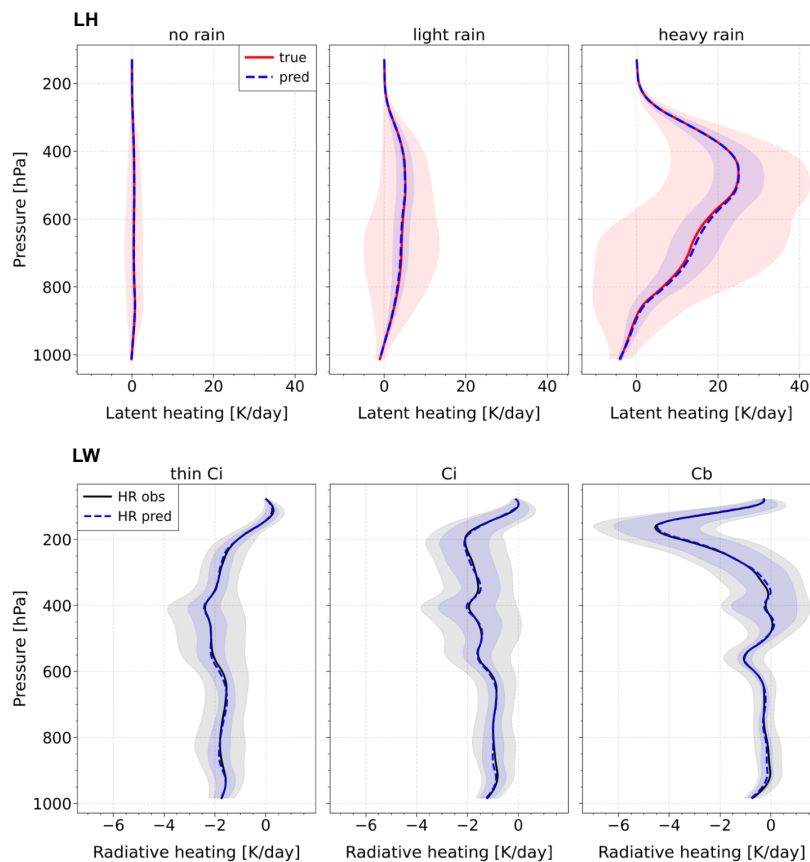
Figure 3. Comparison between predicted (dashed) and observed (solid) latent heating (2004–2013) and radiative heating (2007–2010) of UT clouds, within 30°N–30°S, at a spatial resolution of 0.5°. ANN models were trained on collocated AIRS–TRMM and AIRS–CloudSat–CALIPSO data, respectively. Upper panels: Latent heating rates for different rain rate intensities (no rain, light rain and heavy rain); lower panels: radiative longwave heating rates for different UT cloud types (thin cirrus, cirrus and cumulonimbus). Shaded areas indicate ±67.5 % of the standard deviation, which approximately corresponds to quartiles.

For comparison, lower panels of Fig. 3 show the radiative longwave (LW) heating profiles of the ML-predicted and the original CloudSat–CALIPSO FLXHR profiles (Henderson et al., 2013), separately for thin cirrus, cirrus and high opaque clouds. Here the spread of the predicted and true data is similar, in particular for the optically thicker clouds. Relatively opaque clouds contribute to heating the atmospheric column below by trapping surface emissions while inducing cooling effects in the column above due to excess emission. In contrast, thin cirrus clouds warm the UT by intercepting LW radiation originating from below (Stubenrauch et al., 2021). Notably, above Cb clouds, the cooling is on average -4.5 K day^{-1} around 170 hPa. The minor cooling observed at approximately 550 hPa is attributed to the melting process, which takes place at or just below the freezing level, typically around 5 km above sea level across tropical regions.

3   Construction of the 3D Latent heating dataset by applying the ANN models

235   During the training process, ANN models are tuned to fit the data through continuous adjustment of hyper-parameters by the optimization algorithm to minimize the difference between the predicted output and the true data (loss function). We use these trained models to extend the TRMM–SLH data, which only covers about 3 % of the CIRS observations, to a coverage of 70 % and 77 %, corresponding to the AIRS and IASI swaths over the period 2004–2018 and 2008–2018, respectively. We evaluate the effect of using only specific local times (given by the ANN-predicted LH at observation times of AIRS and IASI), and we

240   compare the vertically integrated LH (LP) to the original temporal sampling of TRMM. At the end of this section, we illustrate differences in the horizontal and vertical structure of LH and RH between La Niña and El Niño.

3.1   Coherence in diurnal variation

Figure 4 shows the vertical LH profiles from the ML production for precipitating clouds. We consider all clouds and specifically UT clouds, separately over ocean and over land. AIRS and IASI observations allow us to examine these profiles at four distinct

245   observation times. The results are coherent with expectations on the diurnal variation:

(1) The shape of the LH profiles averaged over precipitating clouds strongly differs between ocean and land: Over ocean, the mean LH profiles have two peaks, at 450 hPa and at 850 hPa, while over land the LH is mostly produced by UT clouds.

(2) The diurnal spread is larger over land than over ocean, as expected. Over land, the precipitation frequency typically peaks in the late afternoon, whereas over ocean, the diurnal cycle is less pronounced with a maximum occurring in the early morning

250   (e.g., Nesbitt et al., 2000; Dorian, 2014). The observations at 1:30 PM are before the peak of land precipitation, while those at 1:30 AM are before the early morning peak of ocean precipitation. LH also involves the intensity of precipitation, and given that MCSs contribute to over half of intense precipitation (e.g., Roca et al., 2014), we observe the largest peaks at 450 hPa (corresponding to stratiform anvil precipitation) at 9h30 PM over land and at 9:30AM over ocean, respectively, a few hours after convection had started and MCSs could form.

255   (3) In particular over land, we notice a diurnally changing profile shape, with a stronger contribution from lower atmospheric levels at early afternoon, corresponding to the development of cumulo-congestus. Later in the evening, the peak moves higher into the UT, corresponding to stratiform anvils. During night there may be a more complex vertical structure with convection from lower clouds underneath the UT clouds, and LH is minimum in the morning.
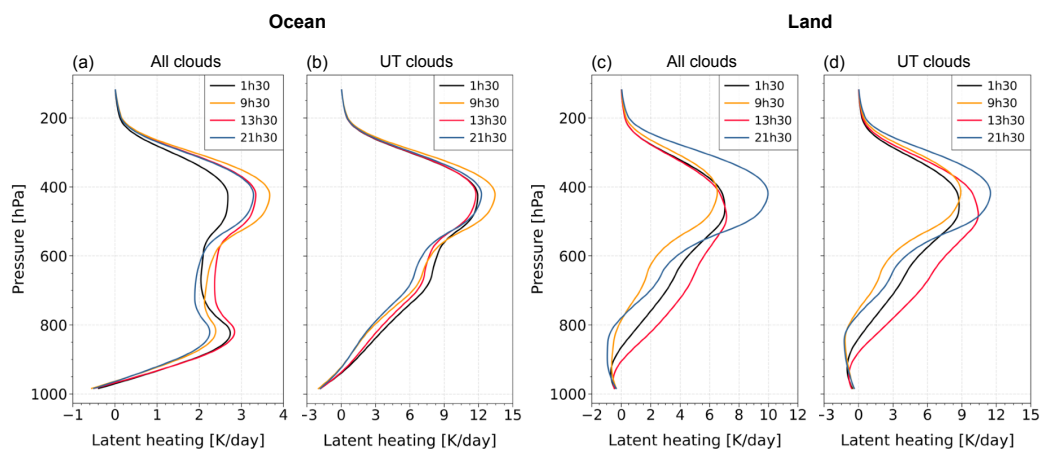
Figure 4. LH profiles of all precipitating cloud scenes (a,c) and precipitating UT clouds (b,d) at 4 observation times (1h30, 9h30 AM/PM), separately over ocean (a,b) and over land (c,d). Data are from the CIRS–ML production during the period 2008–2013, within 30°N–30°S, at a spatial resolution of 0.5°.

3.2 Coherence between TRMM-SLH LP and ML-predicted LP

260   Due to the large diurnal cycle of occurrence and intensity of precipitation over land, the time sampling plays an important role in order to obtain reliable monthly means of LH. Figure 5 compares zonal averages of the ML-derived LH at specific observation times with the original diurnally-sampled TRMM SLH, both vertically integrated, separately over ocean and over land. The collocated TRMM–CIRS data used for the training are displayed to show the quality of the ML-derived zonal means.
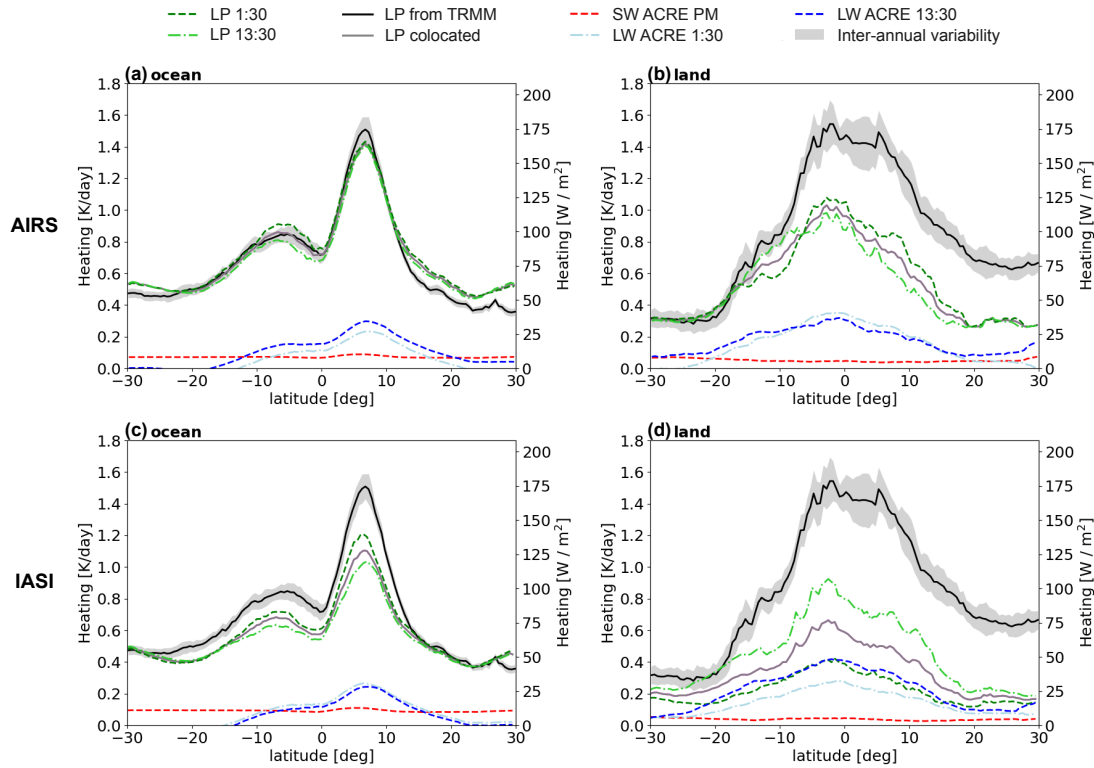
Figure 5. Zonal averages of vertically integrated LH (LP), SW ACRE and LW ACRE at 4 specific observation times (1h30, 9h30 AM/PM) and for TRMM original time sampling, within 30°N–30°S, at a spatial resolution of 0.5°. (a) Heating rates from AIRS over ocean, (b) heating rates from AIRS over land, (c) heating rates from IASI over ocean, (d) heating rates from IASI over land. LP from TRMM data for the period 1999–2014 is represented by a solid black line, with gray shading indicating its inter-annual variability. Pink solid line indicates TRMM–AIRS (2004–2018) or TRMM–IASI (2008–2018) collocated LP. The green dashed line and bright green dash-dotted line represent LP from ML regression using TRMM–AIRS (2004–2018) and TRMM–IASI (2008–2018) as inputs at various observation times (AM, PM). The red dashed line, the bright blue dash-dotted line, and the dark blue dashed line indicate the SW ACRE (24h mean), LW ACRE for AM and PM from AIRS or IASI using ML regressions, respectively.

We note the following points:

265   (1) The vertically integrated LH of the collocated TRMM–AIRS and TRMM–IASI falls between the ML-derived LP at AM and PM of the production. This means that the productions are coherent.

(2) Over ocean, all zonal means of LP show a peak around 5° north of the equator, with a minor broader peak from the equator to approximately 10°S, corresponding to the large LP released over the Pacific warm pool. Over land, there is only one broad peak from about 10°N to 10°S.

270   (3) Overall, the latitudinal behaviour of LP given by AIRS–ML and IASI–ML is consistent with the one given by TRMM with a broader diurnal sampling. It is remarkable that over ocean the zonal averages of LP at 1:30 AM and 1:30 PM agree
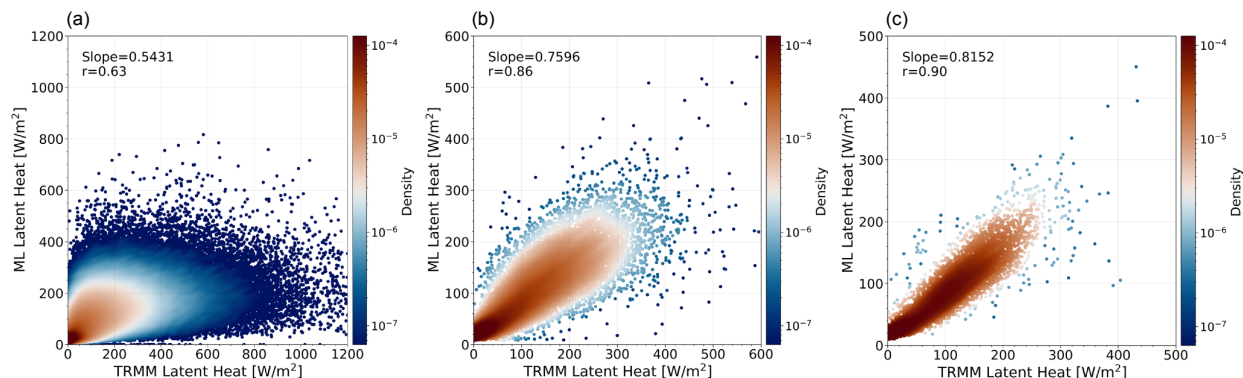
Figure 6. Relationship between monthly means of vertically averaged latent heat of TRMM–SLH LP and of CIRS–ML LP at different spatial scales: per grid cell of (a) 1° latitude × 1° longitude, (b) 5° and (c) 10° (from left to right). Statistics over ocean 10°N–10°S, over the time period from 2004–2013.

very well with those from TRMM. However, over land, as expected, considering LP only at these two observation times underestimates the daily mean LP, because the strong convection in the afternoon is not captured. The effect is the worst at 9:30 AM.

275 Figure 5 also includes zonal averages of vertically integrated atmospheric cloud radiative effects (ACRE), considerably smaller than LP. It is interesting to note that the LW ACRE shows a similar latitudinal behaviour as LP, while the SW ACRE has almost no zonal variation (when averaged over 24h).

To investigate the coherence between monthly averages of TRMM–SLH LP and of CIRS–ML LP in more detail, we examined their relationship at different scales, using averages over grid cells of 1°, 5° and 10°. Differences from a 1-to-1 relationship

280 stem (1) from biases in the CIRS–ML LH and (2) from differences in the sampling of observation times. Since the diurnal sampling of TRMM is not homogeneous, a larger grid cell has a larger probability to include more observations at 1:30 LT. In order to investigate the latter effect, we compare this relationship in two different latitude bands, as according to Negri et al. (2002) the TRMM's revisit cycle strongly varies across regions, with 23 days at the equator and up to 46 days at the highest latitudes. Therefore, to explore this effect of inhomogeneous sampling, we contrasted the results of the two latitudinal bands 10°N–10°S

285 and 20°–30° N/S. We computed the slopes and correlation coefficients between LP of TRMM and CIRS–ML, averaged over 1°, 5° and 10°, for both latitude bands, over ocean. While the slopes increase from 0.54 to 0.82 in the band close to the equator, they vary from 0.44 to 0.77 (not shown) at the higher latitudes with a repeat cycle which is only half as large.

The larger slopes near the equator demonstrate their dependency on the TRMM diurnal sampling variability. Figure 6 presents the results over ocean for 10°N–10°S. The increase of the slopes and the increasing linearity of the scattered points in

290 the CIRS-ML-TRMM LP space with increasing grid cell size show a strong bias reduction and noise reduction when averaging over more observations. At the spatial averaging over 1°, the small slope is related to the fact that the ANN regression does not capture well extreme events, and the relatively noisy relationship is due to the inhomogeneous TRMM sampling at specific

times. Therefore, for larger grid cell sizes the agreement is much better. In summary, the increasing slopes of the relationship between LP of CIRS–ML and TRMM suggest that our ML-expanded LH dataset is suitable at scales larger than about 2.5°
295 (with a slope of 0.7).

3.3 Structure of diabatic heating: Contrasting La Niña and El Niño events

After verifying the ML-derived LH production along the vertical and latitudinal directions, we show that the horizontal patterns produced by this 3D LH dataset for La Nina and El Nino are as expected. Figure 7a–d show geographical maps of LP and ACRE respectively, for two distinct scenarios: La Niña (Jan 2008) and El Niño (Jan 2016). LP is marked by contours while the colours
300 correspond to ACRE values. The LH and CRE profiles, averaged over 30°N–30°S, are given as a function of longitude in Fig. 7e and 7f.

During El Niño (warm phase), sea surface temperatures (SST) are higher than normal in the eastern and central equatorial regions of the Pacific Ocean, leading to increased convection and cloudiness in these regions, which cause an increase in latent heat release. Lower SST in the western Pacific leads to a decrease in convection and cloudiness in the region, resulting in
305 negative LP anomalies. La Niña shows the opposite behaviour (Fig. 7a and 7b).

During La Niña, there is a large, structured band of latent heating in the South Pacific Convergence Zone (SPCZ) (Fig. 7c and 7d), in addition to large LP in the Intertropical Convergence Zone (ITCZ), mostly over the continents. During El Niño, we notice that the maximum distribution of latent heating moves eastward, which happens because the upward branch of the Walker Circulation shifts towards the central Pacific (e.g., Bayr et al., 2018). This is even more evident in Fig. 7e and 7f.
310 Furthermore, there are some regions with negative CRE values at altitudes around 850 hPa, which correspond to the presence of low-level clouds. This effect is more significant during La Niña because convective activity peaks in the western Pacific during La Niña, whereas in the eastern Pacific, with lower SSTs and less convective activity, there is more low-level cloud formation, thereby leading to a negative CRE aloft.
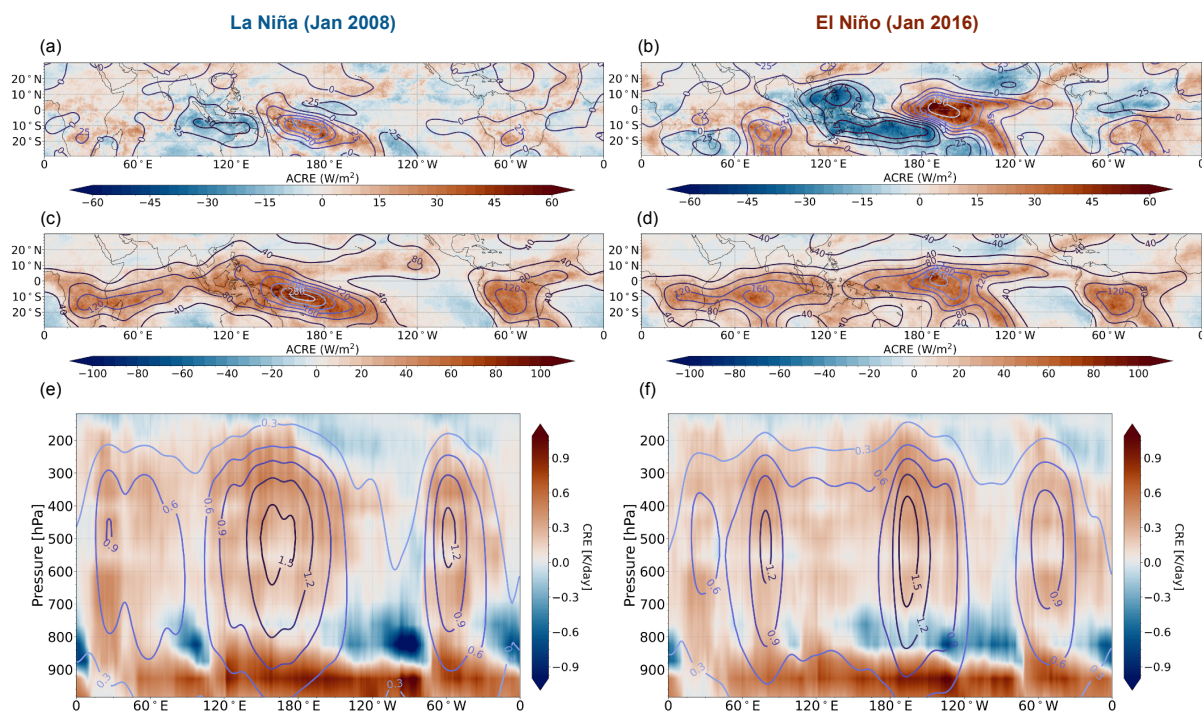
Figure 7. (a) & (b): Maps of anomalies of vertically integrated LH and ACRE during La Niña (Jan 2008) and El Niño (Jan 2016), obtained by subtracting the corresponding 10-year (2008–2018 JAN) averages; (c) & (d): Maps of vertically integrated LH and ACRE during La Niña (Jan 2008) and El Niño (Jan 2016), respectively; (e) & (f): Plots of longitudinal-vertical LH and CRE during La Niña (Jan 2008) and El Niño (Jan 2016), respectively. All data are within $30°N$–$30°S$, at a spatial resolution of $0.5°$. The colorbars represent the ENSO ACRE anomalies (W m^{-2}), ACRE (W m^{-2}) and CRE (K day^{-1}) values from CIRS–ML–Cloudsat–CALIPSO, while contours correspond to vertically integrated ENSO LH anomalies (W m^{-2}), vertically integrated LH (W m^{-2}) and LH values (K day^{-1}) from CIRS–ML–TRMM, at 1h30 AM/PM.
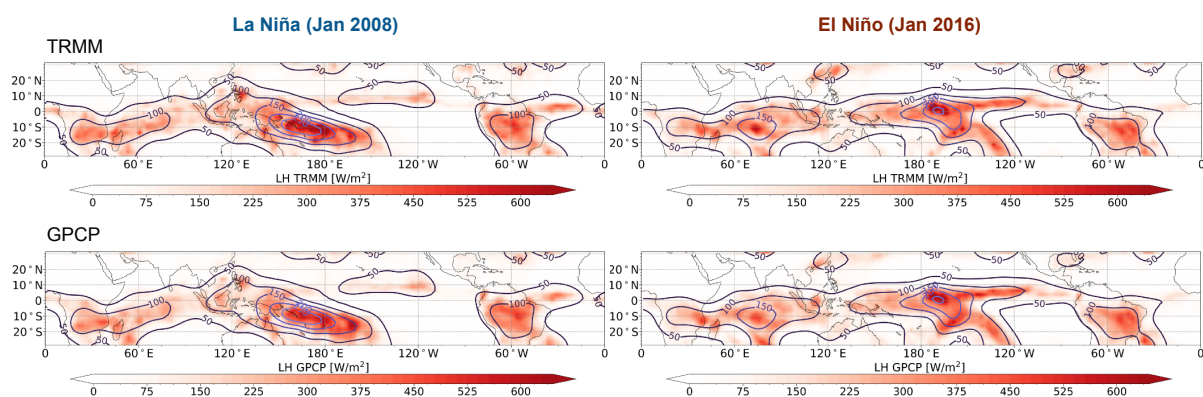
Figure 8. Comparison of horizontal structures between the vertically integrated LH (LP) of CIRS–ML (at 1:30 LT) and those obtained from daily precipitation accumulation of TRMM (upper panels) and GPCP (lower panels) during La Niña (Jan 2008) and El Niño (Jan 2016), within the region of 30°N–30°S, at a spatial resolution of 2.5° × 2.5°. The LP from CIRS–ML is represented by contours, while the colorbars indicate the LP from TRMM and GPCP.

We also assessed the coherence between our predicted LP and the LP calculated using precipitation data from TRMM
(3B42_Daily, Huffman et al., 2007) and the Global Precipitation Climatology Project (GPCP CDR_V2.3, Adler et al., 2016
during the same ENSO events. To facilitate comparison between our ML-derived LP and the precipitation datasets, we esti-
mated $LP = \rho_l L\nu R$, as in L'Ecuyer and Stephens (2007): where ρ_l is the density of liquid water (1000 kg m^{-3}), $L\nu$ is the
latent heat of vaporization of water (2.5×10^6 J kg^{-1}), and R represents the surface rainfall rate (m s^{-1}). Using this formula,
the conversion factor to convert precipitation rates from TRMM and GPCP (mm day^{-1}) to latent heat flux LP (W m^{-2}) is
28.9 W m^{-2}/(mm day^{-1}). Figure 8 shows that the LP computed from GPCP and from TRMM daily accumulated precipitation
agree very well. Moreover, the geographical patterns of our ML-predicted LP align closely with the ones derived from TRMM
and GPCP precipitation data during both La Niña and El Niño phases.

All the above suggests that the horizontal structures of our ML-expanded LP well represent the monthly means of the
LP from other datasets, and strongly reflect the characteristics of ENSO events. In addition, ACRE shows a highly matched
distribution pattern with LP. In other words, larger ACRE distributions are also seen in the regions of larger LP, and therefore
enhancing LP. In section 5 we will explore in more detail the connection between them, in particular at the scale of mesoscale
convective systems (MCS) which needs averages within MCS. Therefore, we describe in the next section the reconstruction of
these MCSs.

4 Construction of mesoscale convective systems

We use the CIRS data to reconstruct UT cloud systems, with a method developed by Protopapadaki et al. (2017) and refined by
Stubenrauch et al. (2023). We consider UT clouds with $P_{cld} < 350$ hPa. The grid cells of 0.5° latitude × 0.5° longitude have to
be covered by at least 90 % of these clouds. Since ubiquitous thin cirrus in the TTL (Tropical Tropopause Layer) connect with
many of the MCS, we exclude for this UT cloud system reconstruction those UT clouds with emissivity smaller than 0.2. First,
grid cells with UT clouds of similar height (within 8 hPa × ln(P_{cld} [hPa])) are merged together into the same system. Then
the size of convective cores is computed within regions of cloud emissivity > 0.93 by the number of grid cells with emissivity
> 0.98. An MCS is defined as an UT cloud system with at least one convective core and the presence of precipitation. The
convective core fraction, given by the ratio of convective core size over MCS size, can be used as a proxy of the maturity stage
(e.g., Stubenrauch et al., 2023).

Since for the cloud system reconstruction the gaps between the orbits have been filled (Protopapadaki et al., 2017), but the
CIRS–ML diabatic heating and precipitation intensity classification have only been extended within the orbits of AIRS and
IASI, we select for the following analyses only systems where the ACRE and LP swaths overlap with the MCS by more than
70 %. Furthermore, we concentrate only on oceanic systems, with less than 10 % of the system being over land. According to
these criteria, we are left with about 26000 MCSs for the period of 2004–2018.
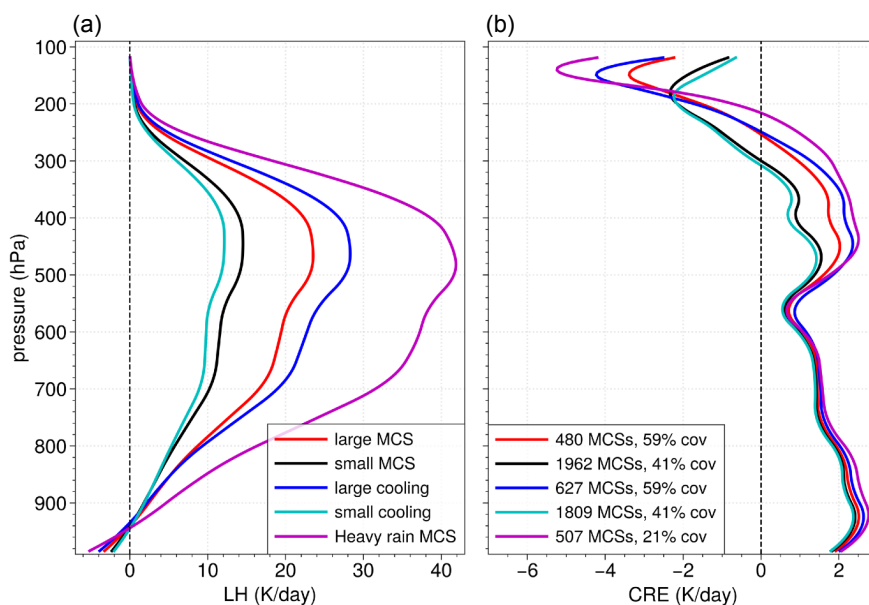
Figure 9. (a) Profiles of latent heating; (b) profiles of radiative heating. Averages over heavily precipitating MCSs (magenta), averages over small (black) and large (red) MCSs, and averages over MCSs with a small (cyan) and large (blue) minimum cooling above the precipitating parts, with thresholds at 10000 km^2 and -7.5 K day^{-1}, respectively. The number and their coverage compared to all MCSs are also given per category. Oceanic systems over the time period 2004–2018, within 25°N–25°S.

In order to test the coherence of the data, we first compare the diabatic profiles of MCSs with different precipitation intensity. Therefore, we explore various proxies of convective intensity: (1) the presence of heavy precipitation (e.g., Takahashi et al., 2021), (2) MCS size (e.g., Roca and Fiolleau, 2020; Stubenrauch et al., 2023, etc) and (3) minimum LW cooling above the precipitating part of the MCS. The latter is directly linked to the opacity.

Figure 9 presents profiles of latent heating and radiative heating averaged over MCSs of similar maturity stage (convective core fraction within the system between 0.6 and 0.8), distinguished by precipitation intensity as described above: Heavily precipitating MCSs (at least more than 5 mm h^{-1} in one grid cell) are shown in magenta, profiles of the MCSs distinguished by their size in black (small) – red (large) and by their minimum cooling above the precipitating parts in cyan (small cooling) – blue (large cooling), with thresholds in MCS size and cooling at 10000 km^2 and -7.5 K day^{-1}, respectively. All profiles show a peak in latent heating at around 450 hPa. This is much higher than one would expect from an isolated convective tower, and is linked to additional stratiform rain of the thick anvils (i.e., Hartmann et al., 1984; Schumacher et al., 2004). The heavily precipitating MCSs, covering about 20 % of the area of all MCSs, produce the largest LH, with a maximum of about 40 K day^{-1} around 450 hPa and a broad shoulder downwards to 700 hPa. MCSs with a large size or a strong cooling above their precipitating parts also produce a larger LH than those of smaller size or with a smaller cooling. The thresholds

chosen above divide the coverage of these categories to approximately 50 %, for both proxies, MCS size and cooling above the
precipitating parts. These two proxies also lead to very similar profiles. Radiative heating adds a small positive heating from
360   200 hPa downward and a cooling above the opaque parts of the MCSs. Cooling and heating are much stronger for heavily
precipitating MCSs, leading to strong vertical gradients. It is interesting to note that the radiative heating profiles of the intense
MCSs according to size and cooling are more similar to the ones of heavily precipitating MCSs than their LH profiles. This
shows, that while intensity is directly related to heavy precipitation, the relation is less direct to MCS size and opacity of the
core.

5   Reinforcement of latent heating by UT cloud radiative heating

Over the deep tropics (15°N–15°S), UT clouds have a net radiative heating effect on the troposphere from 250 hPa downward
by about 0.3 K day^{-1}, and this radiative heating enhances the column-integrated latent heating by about 22 ± 3 % (Li et al.,
2013; Stubenrauch et al., 2021). Regionally and temporally, this enhancement however varies. It was shown that both ACRE
and LP depend on surface temperature (Hartmann and Larson, 2002; Cesana et al., 2019) and column humidity (e.g., Bretherton
370   et al., 2004; Holloway and Neelin, 2009; Masunaga and Bony, 2018; Needham and Randall, 2021; Masunaga and Takahashi,
2024). Therefore, we explore the relationship between latent and radiative heating as a function of these environmental factors
(section 5.1) and then, more specifically, for mesoscale convective systems (section 5.2). Since we found LP more reliable over
ocean, we consider in the following only precipitating clouds over ocean.

5.1   Relationship between LP, ACRE and environment

375   On average, the radiative enhancement ACRE increases with LP, as seen in Fig. 10a and 10b (black curves) and as already
discussed by (Stephens et al., 2024). This increase flattens for LP larger than about 250–500 W m^{-2}. Figure 10a and 10b also
show the relationship between ACRE and LP for different environmental conditions: (1) warm and humid, (2) warm and dry,
(3) cool and humid, (4) cool and dry. These environmental conditions are given by sea surface temperature (SST) and by the
integrated column water vapour (CWV), obtained from the ERA-Interim meteorological reanalyses, and we have defined them
380   as : (1) SST > 302 K and CWV > 60 mm, (2) SST > 302 K and CWV < 45 mm, (3) SST < 298 K and CWV > 60 mm, and (4)
SST < 298 K and CWV < 45 mm.

When stratified by environmental condition, we still observe the increase of ACRE with increasing LP, but for each LP
interval the average ACRE is largest for warm and humid situations and smallest for cool and dry situations. Figure 10a (all
precipitating clouds) and 10b (only precipitating UT clouds), differ mostly for smaller LP as lower clouds do not produce as
385   much LP. The averages of ACRE in dry situations at these smaller LP show that UT clouds radiatively heat the atmosphere,
while low-level clouds cool the atmosphere (above them). For UT clouds with LP greater than 500 W m^{-2}, ACRE differences
between cool-dry and warm-humid conditions increase from 30 to 50 W m^{-2} with increasing LP. It is interesting to note that
ACRE is similar between warm-dry and cool-humid conditions, and both are quite close to ACRE in warm-humid situations.
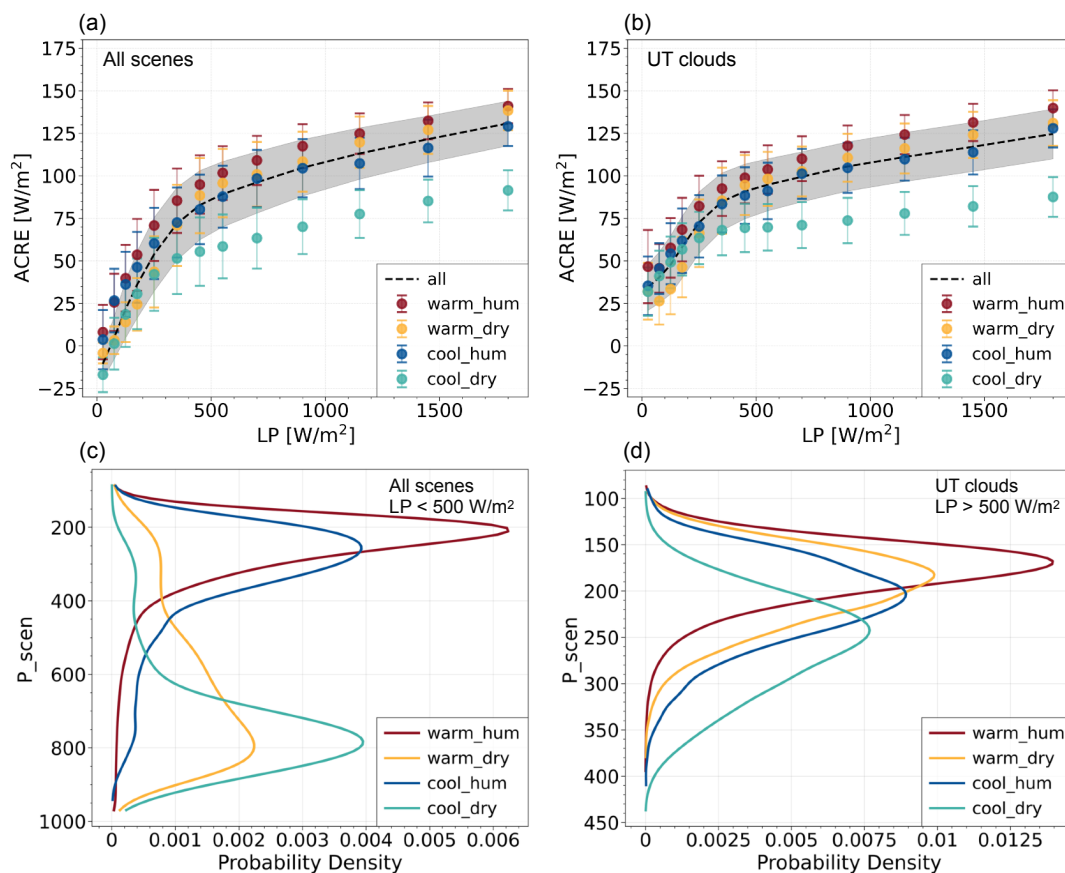
Figure 10. (a) & (b): Relation between LP and ACRE of precipitating clouds (black) and for four specific environments (cool-warm, humid-dry), for all cloud scenes and for UT clouds, respectively. Shaded areas and error bars indicate $\pm 67.5\%$ of the standard deviation. (c) & (d): probability density of cloud pressure for these different environments, for all cloud scenes and for UT clouds, respectively. All data are from the period 2004–2013, within $30°\text{N}–30°\text{S}$, at a spatial resolution of $2.5° \times 2.5°$, over ocean.

This means that for UT clouds releasing large latent heat, the SST has a large impact on ACRE in dry environments, while in
390   humid conditions the SST has no great impact on ACRE.

Now how can UT clouds which release the same latent heat have such a different ACRE? The cloud height in these different environments plays a key role, as shown by the cloud top pressure distributions in Fig.10c and 10d, respectively for all precipitating clouds with small LP (< 500 W m^{-2}) and only precipitating UT clouds with large LP (> 500 W m^{-2}). A larger ACRE can be explained by a higher cloud height (lower cloud top pressure): The highest clouds (peak at 170 hPa or about 15 km) are
395   situated in a warm and humid environment and the lowest UT clouds (peak at 240 hPa or about 11 km) are situated in a cool
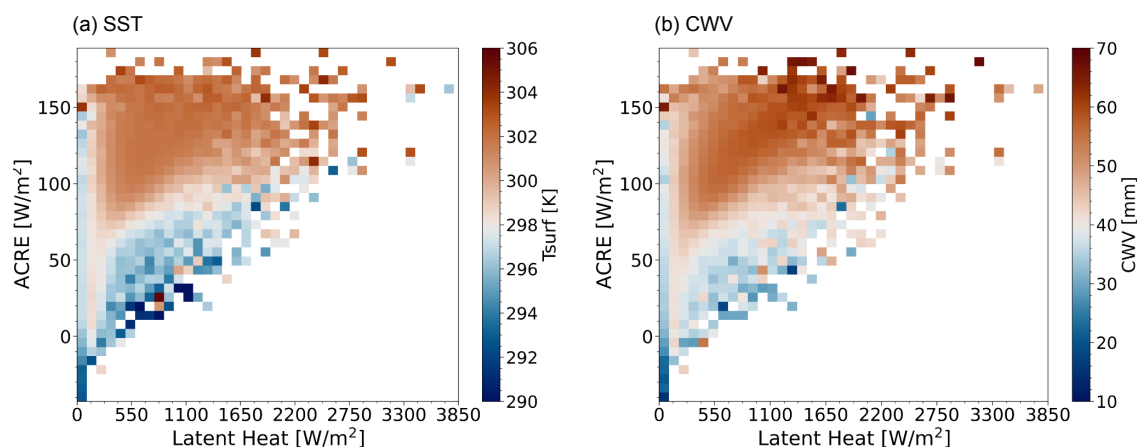
Figure 11. Averages of (a) SST and (b) CWV as function of LP and ACRE released by precipitating UT clouds over the ocean, for the period 2004-2013, spanning 30°N to 30°S, at a spatial resolution of 2.5°. LP and ACRE are from CIRS–ML, while SST and CWV are from ERA-Interim at 1:30 AM/PM local time. Each square corresponds to a specific LP–ACRE interval.

and dry environment, the cloud height distributions in cool-humid and warm-dry environments are situated between those in warm-humid and cool-dry environments, with each being progressively lower than in the warm-humid environment.

For clouds which only produce small latent heat, humidity plays a dominant role in enhancing ACRE (Fig. 10a), as already pointed out by Needham and Randall (2021). Again this is linked to the distribution of cloud height (Fig. 10c): UT clouds are much more frequent in humid than in dry regions, while lower-level clouds exist mostly in dry regions. Moreover, when SST increases, low cloud cover decreases, reducing the reflection of shortwave radiation by clouds and allowing more sunlight to reach the surface, which enhances surface warming. Therefore, the cooling effect of warm-dry low clouds is weaker compared to low clouds in cool-dry environments (Cesana et al., 2019).

Why does cloud height differ under varying SST–CWV conditions? Humid environments increase the buoyancy of convective clouds, which allows clouds to reach greater heights (Holloway and Neelin, 2009), confirmed by Fig. 10b. In dry environments, the lower water vapor content results in smaller plume buoyancies, limiting convection and preventing clouds from reaching the same height as in humid conditions. However, even with lower humidity, higher SST provide enough energy to lift air upwards, forming taller clouds. This explains why cloud heights and ACRE in humid and warm-dry conditions are similar, while both cloud heights and ACRE are significantly lower in a cool-dry condition.

When considering the distribution of UT clouds in the LP–ACRE plane, with SST and CWV averaged over each interval in LP and ACRE, as shown in Fig. 11a and 11b, respectively, we observe a very large spread in ACRE for small LP, which gradually is reduced towards larger LP. As one expects that UT clouds heat the atmosphere, the occurrence of negative ACRE values for LP values less than 500 W m^{-2} should correspond to thin cirrus with lower precipitating clouds underneath. In this case, the CIRS cloud retrieval itself only provides the properties of the uppermost cloud.
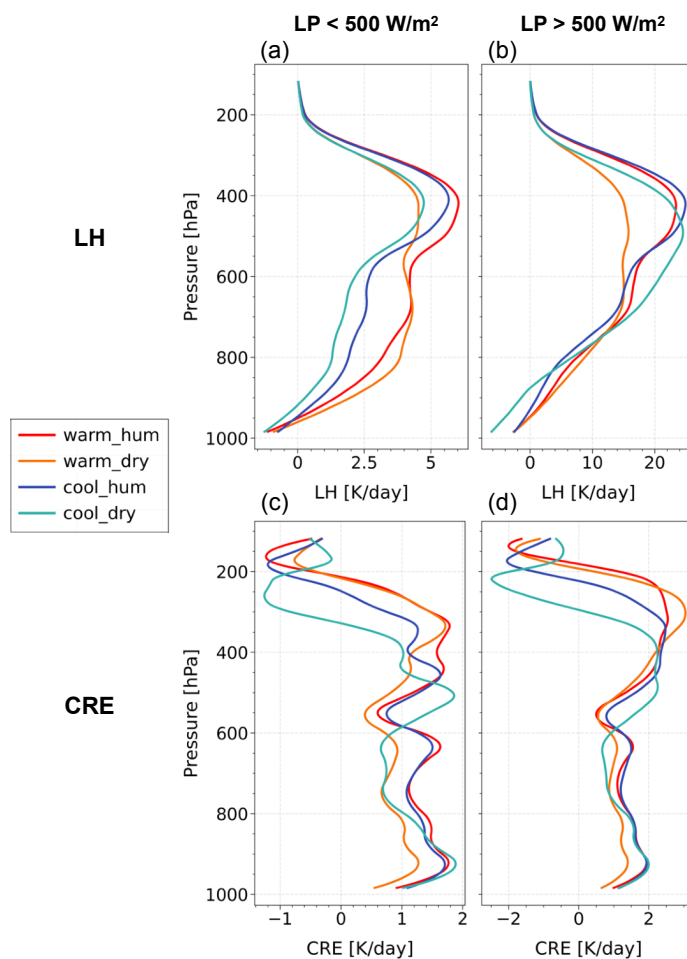
Figure 12. LH (top panels) and CRE (bottom panels) profiles of precipitating UT clouds, segmented by an LP threshold of 500 W/m^2 across the environments of Fig. 10. All data are from the period 2004–2013, within 30°N–30°S, at a spatial resolution of 2.5° × 2.5°, over ocean.

These occurrences in the LP–ACRE plane and their associated average environments can be compared to the phase diagram which Masunaga and Takahashi (2024, Fig. 6) have obtained by an energy and humidity budget analysis of the Lagrangian evolution of convection. According to Fig. 11a and 11b, UT clouds in the more or less warm-humid conditions correspond mostly to a mid-heavy convective regime, while the bottom-heavy convection regime, with small LP and a widely spread ACRE, occurs in a cool-dry environment, with UT clouds on top of lower convection. For larger LP, the cases of low ACRE should correspond to the top-heavy convective regime, and these are also associated to a cool-dry environment. The results are robust, when averaged over 5° (Fig. S7).

In order to explain the smaller ACRE in the cooler and drier environment, which corresponds to 'top-heavy' convective regimes, Fig. 12 shows the heating profiles of the UT clouds for the environments defined above, in two LP intervals. Indeed,

for the small LP interval and the cool environments, the LH profiles seem to be dominated by stratiform rain, with a relatively narrow LH peak around 410 hPa, while the LH profiles for the warmer environments also show a heating in the mid- and lower part of the troposphere. For larger LP, the LH profiles are more similar between these different environments, with an increasing and broadening of the peak towards the mid- and lower troposphere. This indicates either an increase of the latent heating produced by the convective cores (mid-heavy) or additional heating by the bottom-heavy lower convection underneath the anvils (as suggested by Masunaga and Takahashi (2024)). The relatively small ACRE in the cool-dry environment in Fig. 11 corresponds to a radiative heating below a height of 450 hPa and a relatively large and broad cooling above this height. The reason why ACRE is smaller under these environmental conditions is that the UT clouds are lower in height (as shown above), and that the cooling above them is more pronounced. The larger cooling can be explained by the fact that lower clouds are warmer, thus they emit more LW radiation and the atmosphere above cools more. The larger cooling also leads to a slightly larger vertical gradient in radiative heating. The smaller height may be interpreted as anvils of convective systems having descended at a later stage of their life cycle or as relatively thick clouds with diffusive tops, for which the retrieved (radiative) height may be deeper within the cloud because of very small ice water content in the upper part of the cloud (e.g., Liao et al., 1995; Stubenrauch et al., 2010, 2017).

5.2 Diabatic heating of MCS

Deep convection in the tropics leads to a large outflow of anvil clouds. The radiative heating of these UT clouds originating from convection enhances the latent heating associated with precipitation and thereby strengthens the circulation Stephens et al. (2024). In the following, we explore the relationship between LH and RH within the MCSs.
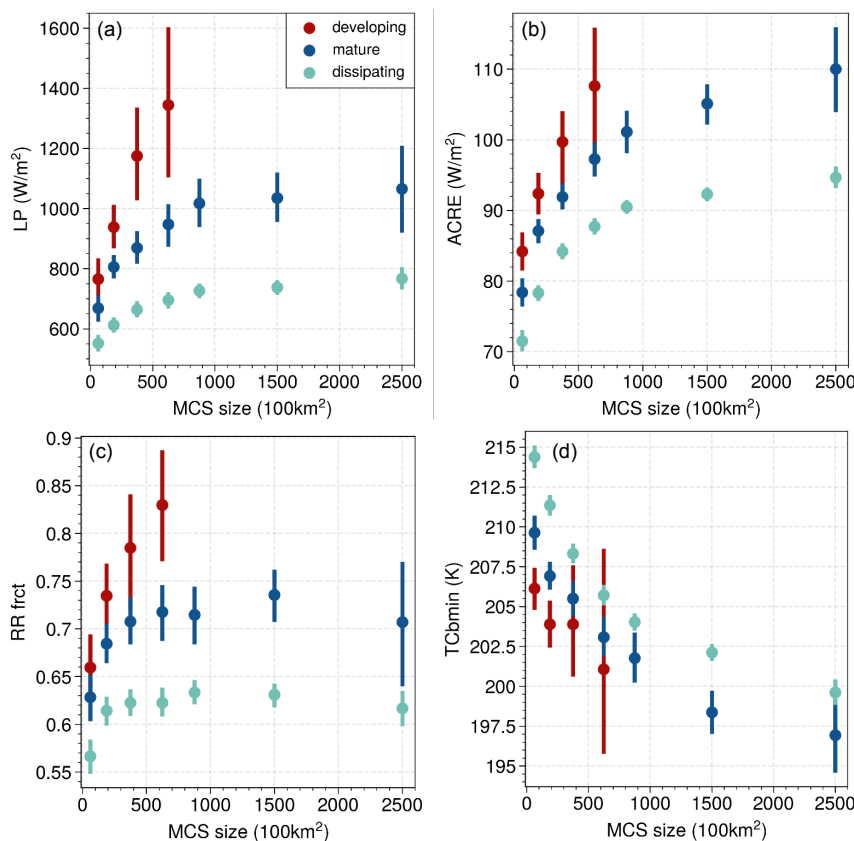
Figure 13. LP (a), ACRE (b), rainy area fraction (c) and minimum temperature within the convective core per MCS (d), as a function of the MCS size, separately for developing, mature and dissipating MCSs (distinguished by convective core fraction: 0.6–0.9, 0.4–0.6 and 0.2–0.4, respectively). MCSs over ocean, 1:30 LT, 2004–2018, 25°N–25°S.

First, we study how LP and ACRE change with the size of the MCS. It has been shown that the horizontal extent of the MCS depends on the intensity and organization of convection, but it also changes during the life cycle of the MCS (e.g., Machado et al., 1998; Takahashi and Luo, 2014; Protopapadaki et al., 2017) Therefore, we analyze the MCS properties separately at 445 different life stages: developing, mature and dissipating, defined by convective core fractions of 0.6–0.9, 0.4–0.6 and 0.2–0.4, respectively. Figure 13 shows that both LP and ACRE increase with MCS size, as expected from Fig. 9. The increase flattens for larger MCS size. Furthermore, for a similar MCS size, LP and ACRE decrease from developing towards dissipating stage, as expected (e.g., Bouniol et al., 2021; Takahashi et al., 2021; Elsaesser et al., 2022). These behaviors are in line with those of the fraction of precipitation area within the MCS and the minimum temperature within the convective core, respectively: The 450 fraction of precipitating area increases similarly as LP with MCS size, and the core top temperature decreases with MCS size, which explains the increasing ACRE. On the other hand, the slightly decreasing anvil emissivity (not shown) should dampen the ACRE increase.
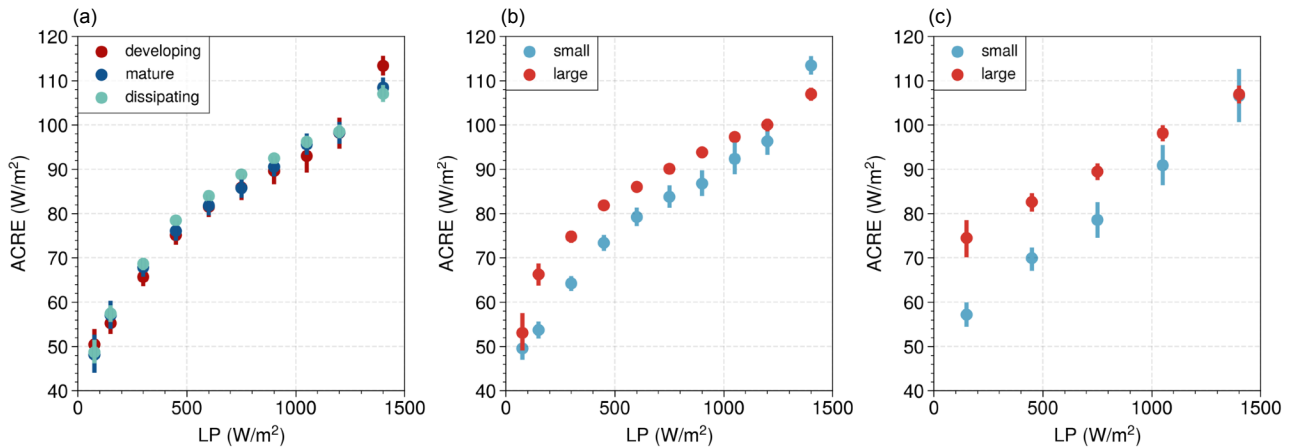
Figure 14. Relationship between radiative enhancement ACRE and precipitation intensity LP, averaged per MCS:(a) for different life stages (distinguished by convective core fraction: 0.6–0.9, 0.4–0.6 and 0.2–0.4, respectively), (b) for MCS sizes smaller than 7500 km^2 and larger than 15000 km^2, (c) for MCS sizes smaller than 7500 km^2 and larger than 15000 km^2 for mature MCSs (convective core fraction 0.4–0.6). MCSs over ocean, 1:30 LT, 2004–2018, 25°N–25°S.

The relationship between precipitation intensity (LP) and radiative enhancement (ACRE) shows on average no distinction between developing, mature and dissipating stage, as shown in Fig. 14a. The average ACRE per MCS increases steadily with

455   the average LP per MCS, from about 50 W m^{-2}to 115 W m^{-2}. However, when separating small and large MCSs, we observe in Fig. 14b a systematic, slightly larger ACRE for systems of similar average rain intensity, except for the most intense systems. These larger systems have on average a smaller core fraction than the larger ones (0.35 compared to 0.60).

In order to isolate the effect of convective organization, we therefore only select mature MCSs for the comparison between smaller, less organized and larger, more organized MCSs at similar average rain intensity. Fig. 14c shows a linear relationship

460   between mean ACRE and mean LP per mature MCS, for both small and large systems. The difference in ACRE, with about 20 km^2 for a small rain intensity, decreases with increasing rain intensity, as ACRE saturates. Furthermore, it is interesting to note that the core top temperature is relatively stable for the smaller MCSs (215 K to 210 K), while the one of the larger MCSs decreases steadily from 215 K to 198 K (not shown). This means that the mean ACRE difference between these systems is largest when their core top temperatures are similar. So, in this case it is not the height of the systems which is responsible

465   for the enhanced ACRE, but probably their vertical structure. The shapes of the radiative heating profiles of these mature MCSs in Fig. 15b confirm this. This Figure reveals first that for both small and large MCSs the vertical gradients increase, with increasing cooling above and increasing heating below the MCSs. Furthermore, in each of the three chosen LP categories the vertical gradient of the larger, more organized systems is larger compared to the smaller MCSs. This additional ACRE
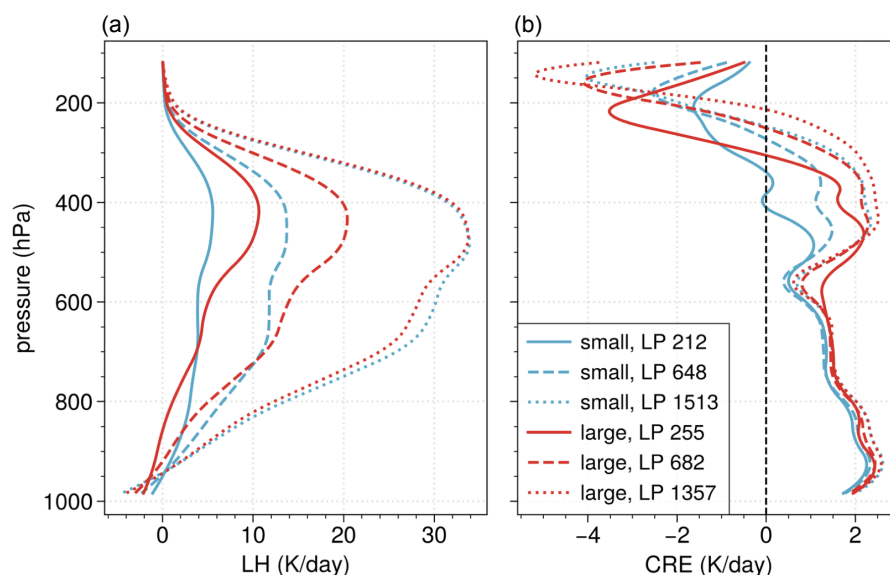
Figure 15. Profiles of latent heating (a) and of cloud radiative effect (b) averaged per mature MCS (core fraction 0.4–0.6) for three LP intervals, with mean values of approximately 220, 660 and 1400 W m^{-2} (LP means in the legend in W m^{-2}), separately for MCS sizes smaller than 7500 km^2 and larger than 15000 km^2. MCSs over ocean, 1:30 LT, 2004–2018, 25°N–25°S.

and larger vertical heating gradient then may further support stronger and more sustained convective intensity by enhancing
470 updrafts, maintaining the system, and modifying the larger-scale environment.

As expected (e.g., Houze, 2004), the shapes of the LH profiles of the mature MCSs in Fig. 15a show that larger, more organized MCSs have a larger contribution of stratiform rain than the smaller MCSs, except for the most precipitating ones which show a large heating through the whole atmosphere. It needs more detailed studies at a better spatial resolution to understand if the heating in the middle troposphere comes from more productive cores or from anvil with precipitating systems
475 underneath, as already suggested by Masunaga and Takahashi (2024).

6 Conclusions and Outlook

In this article we explored the relationship between latent and radiative heating rates in the tropics. These profiles have been obtained from active instruments, which have a sparse sampling. In order to expand these heating rates in space and time, we used techniques based on artificial neural networks (ANN). While the radiative heating and a precipitation classification have
480 already been expanded earlier (CIRS–ML dataset, Stubenrauch et al., 2021, 2023), we presented here the extension of the latent heating rates. We assessed the consistency of the extended LH and RH fields. Finally, we examined the relationship between latent and radiative heating for different environments and for MCSs.

To expand the SLH latent heating derived from TRMM radar measurements (Shige et al., 2009), we used similar neural network regression methods and inputs as for the radiative heating expansion, but trained on collocated AIRS–TRMM and IASI–TRMM data, respectively. While for the radiative heating rates the predicted averages as well as their variability match well those of the original CloudSat–CALIPSO FLXHR data, the predicted LH profiles show a very good agreement of the means with the target TRMM LH profiles. However, the range of the predicted values is much narrower than the one of the target data, likely due to insufficient input information and to a coarse spatial scale (0.5°). Though the prediction is only slightly better than a simple class mean, this heating rate expansion allows us to study horizontal fields of diabatic heating, in particular of MCSs.

We reconstructed the 3D latent heating fields at four observation times, at 1:30 AM / PM LT (AIRS) over the period 2004–2018 and at 9:30 AM/PM LT (IASI) over the period 2008–2018. The horizontal structure of the vertically integrated LH (LP) closely matches the one from precipitation obtained from TRMM and GPCP, and reflects well the characteristics of ENSO events. Furthermore, the geographical maps show a close association between LP and the vertically integrated, atmospheric cloud radiative effect (ACRE).

The zonal averages of LP at 1:30 AM and PM LT align well with those from the full diurnal sampling of TRMM–SLH over ocean. However, over land, the daily mean LP is underestimated because the strong convection in the late afternoon is not captured at these observation times. The observation times of IASI underestimate the daily mean LP over both ocean and land. Therefore, we have performed all relationship analyses on the heating fields from AIRS–CIRS–ML over ocean.

The slopes between the monthly averages of TRMM–SLH LP and CIRS–ML LP over ocean increase from 0.54 to 0.82 for scales between 1° and 10°, with slopes of 0.68 and 0.76 for 2.5° and 5°, respectively. We have used the CIRS-ML-expanded LH dataset for studies over ocean at scales of 2.5°. While this LH may be slightly underestimated for larger values of LP, the results are robust when comparing with those averaged at 5°.

The main purpose of this article was to study the relationship between latent and radiative heating for UT clouds, first under different environments characterized by sea surface temperature (SST) and column humidity (CWV), and then within MCSs.

For a similar rain intensity, given by LP, ACRE is generally largest in warm-humid conditions and smallest in cool-dry conditions, which is essentially linked to higher and lower cloud height, respectively. For UT clouds releasing large latent heat, SST has a larger impact on ACRE in dry than in humid environments. On the other hand, for lower clouds, producing relatively small latent heat, humidity plays a large role in the enhanced ACRE.

The distribution of UT clouds in the LP–ACRE plane shows a large spread in ACRE for small LP, which is gradually reduced towards larger LP. Compared to the phase diagram in (Masunaga and Takahashi, 2024), the UT clouds in the more or less warm-humid conditions correspond mostly to mid-heavy convective regimes. The cool-dry environments are linked on one hand to the bottom-heavy convection regimes with small LP and a widely spread ACRE, and on the other hand, for larger LP and smaller ACRE, to the top-heavy convective regimes. The smaller ACRE can be explained by a slightly larger cooling above the clouds and a smaller (radiative) height of these clouds. The smaller CIRS-retrieved height may be interpreted as anvils of convective systems having descended at a later stage of their life cycle or as relatively thick clouds with diffusive tops,

for which the retrieved (radiative) height may be deeper within the cloud because of very small ice water content in the upper part of the cloud.

For MCSs, the relationship between LP and ACRE shows no difference between developing, mature and dissipating stage.
520   The mean ACRE per MCS increases steadily with the mean LP per MCS, from about 50 W m^{-2} to 115 W m^{-2}.

Convective organization enhances ACRE by up to 20 W m^{-2}. The effect is decreasing towards larger rain intensities, as ACRE saturates. This was revealed when comparing ACRE for mature MCSs (defined by core fraction within the system) between smaller, less organized and larger, more organized MCSs at similar average rain intensity. This time, the height of the systems is not responsible for the enhanced ACRE. Furthermore, while in general the vertical gradient of the radiative heating
525   of these systems increases with their average rain intensity (LP), for a similar LP it is always larger for the more organized systems. This additional ACRE and larger vertical heating gradient then may further support stronger and more sustained convective intensity by enhancing updrafts, maintaining the system, and modifying the larger-scale environment.

As expected, the shapes of the LH profiles of mature MCSs show that larger, more organized MCSs have a larger contribution of stratiform rain than the smaller MCSs.
530   Future studies should consider also the environment around the MCSs and furthermore the time dimension. The latter can be achieved by combining the CIRS–ML heating rates with deep convective cloud systems, using a better spatial and temporal resolution (Fiolleau and Roca, 2013; Takahashi et al., 2021), providing additional parameters such as their life stage, lifetime, and maximum size during their lifetime. The distribution of the UT clouds and their associated environment in the LP–ACRE plane can also be used to evaluate climate simulations.

535 *Data availability.* The TRMM latent heating rates used in this study are from the Tropical Rainfall Measuring Mission (TRMM) dataset: GPM PR on TRMM Spectral Latent Heating Profiles L3 1 Day 0.5° × 0.5° V06, provided by the Goddard Earth Sciences Data and Information Services Center (GES DISC), available at https://doi.org/10.5067/GPM/PR/TRMM/SLH/3A-DAY/06 (Shige et al., 2009). The CIRS-ML radiative heating rates, vertical cloud structure, and rain rate classification data are from the Global Energy and Exchanges Process Evaluation Studies (GEWEX PROES), accessible at https://gewex-utcc-proes.aeris-data.fr/. The TRMM (TMPA) Precipitation L3 1 Day

540 0.25° × 0.25° V7 dataset, used for the comparison of LH horizontal structure with ML-expanded LH, is also available from GES DISC (https://disc.sfc.nasa.gov/datacollection/TRMM_3B42_Daily_7.html). The Global Precipitation Climatology Project (GPCP) Monthly Precipitation Climate Data Record (CDR) is provided by NOAA's National Centers for Environmental Information (doi:10.7289/V56971M6).

Author contributions. XC developed and evaluated the ANN models for the expansion of LH, performed the analysis of the expanded LH and RH data, wrote the main sections of the manuscript, and produced the figures. CJS conducted the cloud-system-related analysis, wrote

545 Section 5.2, generated the corresponding figures, and made substantial contributions to optimizing and revising the manuscript. GM analyzed the zonal averages of vertically integrated diabatic heating, produced Figure 5 in Section 3, and contributed to the overall improvements of the manuscript.

Competing interests. The authors declare that they have no conflict of interest.

Acknowledgements. We gratefully acknowledge the efforts and collaboration of the AIRS, CALIPSO, CloudSat, IASI, and TRMM science

550 teams in providing the datasets used in this study. We also extend our thanks to the engineers and space agencies whose work ensures the consistent quality of these data. The computational resources provided by IPSL ESPRI Mesocenter were instrumental to the completion of this work. We also appreciate the technical support provided by Jeremie Trules during the transition to a new remote server. Special thanks go to Camille Risi, Hirohiko Masunaga, and Laurent ZX Li for their insightful discussions. Finally, we would like to acknowledge the use of Fabio Crameri's "Scientific Colour Maps" (Crameri et al., 2020) in the preparation of some of our figures, which adhere to principles

555 of readability and accessibility in scientific visualization. This work has been supported by the China Scholarship Council (CSC) program (Grant No. 202208070008), the French National Centre for Scientific Research (CNRS) and the Centre National d'Études Spatiales (CNES).

References

Adler, R., Wang, J.-J., Sapiano, M., Huffman, G., Chiu, L., Xie, P. P., Ferraro, R., Schneider, U., Becker, A., Bolvin, D., Nelkin, E., Gu, G., and Program, N. C.: Global Precipitation Climatology Project (GPCP) Climate Data Record (CDR), Version 2.3 (Monthly), https://doi.org/10.7289/V56971M6, 2016.

August, T., Klaes, D., Schlüssel, P., Hultberg, T., Crapeau, M., Arriaga, A., O'Carroll, A., Coppens, D., Munro, R., and Calbet, X.: IASI on Metop-A: Operational Level 2 retrievals after five years in orbit, Journal of Quantitative Spectroscopy and Radiative Transfer, 113, 1340–1371, https://doi.org/https://doi.org/10.1016/j.jqsrt.2012.02.028, 2012.

Bayr, T., Latif, M., Dommenget, D., Wengel, C., Harlaß, J., and Park, W.: Mean-state dependence of ENSO atmospheric feedbacks in climate models, Climate Dynamics, 50, 3171–3194, https://doi.org/10.1007/s00382-017-3799-2, 2018.

Bergman, J. W. and Hendon, H. H.: Cloud Radiative Forcing of the Low-Latitude Tropospheric Circulation: Linear Calculations, Journal of the Atmospheric Sciences, 57, 2225 – 2245, https://doi.org/10.1175/1520-0469(2000)057<2225:CRFOTL>2.0.CO;2, 2000.

Bouniol, D., Roca, R., Fiolleau, T., and Raberanto, P.: Life Cycle–Resolved Observation of Radiative Properties of Mesoscale Convective Systems, Journal of Applied Meteorology and Climatology, 60, 1091 – 1104, https://doi.org/10.1175/JAMC-D-20-0244.1, 2021.

Bretherton, C. S., Peters, M. E., and Back, L. E.: Relationships between Water Vapor Path and Precipitation over the Tropical Oceans, Journal of Climate, 17, 1517 – 1528, https://doi.org/10.1175/1520-0442(2004)017<1517:RBWVPA>2.0.CO;2, 2004.

Cesana, G., Del Genio, A. D., Ackerman, A. S., Kelley, M., Elsaesser, G., Fridlind, A. M., Cheng, Y., and Yao, M.-S.: Evaluating models' response of tropical low clouds to SST forcings using CALIPSO observations, Atmospheric Chemistry and Physics, 19, 2813–2832, https://doi.org/10.5194/acp-19-2813-2019, 2019.

Chahine, M. T., Pagano, T. S., Aumann, H. H., Atlas, R., Barnet, C., Blaisdell, J., Chen, L., Divakarla, M., Fetzer, E. J., Goldberg, M., Gautier, C., Granger, S., Hannon, S., Irion, F. W., Kakar, R., Kalnay, E., Lambrigtsen, B. H., Lee, S.-Y., Marshall, J. L., McMillan, W. W., McMillin, L., Olsen, E. T., Revercomb, H., Rosenkranz, P., Smith, W. L., Staelin, D., Strow, L. L., Susskind, J., Tobin, D., Wolf, W., and Zhou, L.: AIRS: Improving Weather Forecasting and Providing New Data on Greenhouse Gases, Bulletin of the American Meteorological Society, 87, 911 – 926, https://doi.org/10.1175/BAMS-87-7-911, 2006.

Crameri, F., Shephard, G., and Heron, P.: The misuse of colour in science communication, Nature Communications, 11, https://doi.org/10.1038/s41467-020-19160-7, 2020.

Dee, D. P., Uppala, S. M., Simmons, A. J., Berrisford, P., Poli, P., Kobayashi, S., Andrae, U., Balmaseda, M., Balsamo, G., Bauer, d. P., et al.: The ERA-Interim reanalysis: Configuration and performance of the data assimilation system, Quarterly Journal of the royal meteorological society, 137, 553–597, https://doi.org/10.1002/qj.828, 2011.

Dorian, T. A.: Spatial and temporal variability of latent heating in the tropics using TRMM observations, Master's thesis, University of Wisconsin–Madison, 2014.

Elsaesser, G. S., Roca, R., Fiolleau, T., Del Genio, A. D., and Wu, J.: A Simple Model for Tropical Convective Cloud Shield Area Growth and Decay Rates Informed by Geostationary IR, GPM, and Aqua/AIRS Satellite Data, Journal of Geophysical Research: Atmospheres, 127, e2021JD035 599, https://doi.org/https://doi.org/10.1029/2021JD035599, 2022.

Feofilov, A. G. and Stubenrauch, C. J.: Diurnal variation of high-level clouds from the synergy of AIRS and IASI space-borne infrared sounders, Atmospheric Chemistry and Physics, 19, 13 957–13 972, https://doi.org/10.5194/acp-19-13957-2019, 2019.

Fiolleau, T. and Roca, R.: An Algorithm for the Detection and Tracking of Tropical Mesoscale Convective Systems Using Infrared Images From Geostationary Satellite, Geoscience and Remote Sensing, IEEE Transactions on, 51, 4302–4315, https://doi.org/10.1109/TGRS.2012.2227762, 2013.

595 Gill, A. E.: Some simple solutions for heat-induced tropical circulation, Quarterly Journal of the Royal Meteorological Society, 106, 447–462, https://doi.org/https://doi.org/10.1002/qj.49710644905, 1980.

Hagos, S., Zhang, C., Tao, W.-K., Lang, S., Takayabu, Y. N., Shige, S., Katsumata, M., Olson, B., and L'Ecuyer, T.: Estimates of Tropical Diabatic Heating Profiles: Commonalities and Uncertainties, Journal of Climate, 23, 542 – 558, https://doi.org/10.1175/2009JCLI3025.1, 2010.

600 Hartmann, D. L. and Larson, K.: An important constraint on tropical cloud - climate feedback, Geophysical Research Letters, 29, 12–1–12–4, https://doi.org/https://doi.org/10.1029/2002GL015835, 2002.

Hartmann, D. L., Hendon, H. H., and Houze, R. A.: Some Implications of the Mesoscale Circulations in Tropical Cloud Clusters for Large-Scale Dynamics and Climate, Journal of Atmospheric Sciences, 41, 113 – 121, https://doi.org/10.1175/1520-0469(1984)041<0113:SIOTMC>2.0.CO;2, 1984.

605 Haynes, J. M., L'Ecuyer, T. S., Stephens, G. L., Miller, S. D., Mitrescu, C., Wood, N. B., and Tanelli, S.: Rainfall retrieval over the ocean with spaceborne W-band radar, Journal of Geophysical Research: Atmospheres, 114, https://doi.org/10.1029/2008JD009973, 2009.

Henderson, D. S., L'Ecuyer, T., Stephens, G., Partain, P., and Sekiguchi, M.: A Multisensor Perspective on the Radiative Impacts of Clouds and Aerosols, Journal of Applied Meteorology and Climatology, 52, 853 – 871, https://doi.org/10.1175/JAMC-D-12-025.1, 2013.

Hilton, F., Armante, R., August, T., Barnet, C., Bouchard, A., Camy-Peyret, C., Capelle, V., Clarisse, L., Clerbaux, C., Coheur, P.-F., et al.:
610 Hyperspectral Earth observation from IASI: Five years of accomplishments, Bulletin of the American Meteorological Society, 93, 347–370, https://doi.org/10.1175/BAMS-D-11-00027.1, 2012.

Holloway, C. E. and Neelin, J. D.: Moisture Vertical Structure, Column Water Vapor, and Tropical Deep Convection, Journal of the Atmospheric Sciences, 66, 1665 – 1683, https://doi.org/10.1175/2008JAS2806.1, 2009.

Houze, R. A.: Mesoscale convective systems, Reviews of Geophysics, 42, RG4003, https://doi.org/10.1029/2004RG000150, 2004.

615 Houze, R. A. and Hobbs, P. V.: Organization and Structure of Precipitating Cloud Systems, in: Advances in Geophysics, edited by Saltzman, B., vol. 24, pp. 225–315, Elsevier, https://doi.org/https://doi.org/10.1016/S0065-2687(08)60521-X, 1982.

Houze Jr., R. A., Rasmussen, K. L., Zuluaga, M. D., and Brodzik, S. R.: The variable nature of convection in the tropics and subtropics: A legacy of 16 years of the Tropical Rainfall Measuring Mission satellite, Reviews of Geophysics, 53, 994–1021, https://doi.org/https://doi.org/10.1002/2015RG000488, 2015.

620 Huffman, G. J., Bolvin, D. T., Nelkin, E. J., Wolff, D. B., Adler, R. F., Gu, G., Hong, Y., Bowman, K. P., and Stocker, E. F.: The TRMM Multisatellite Precipitation Analysis (TMPA): Quasi-Global, Multiyear, Combined-Sensor Precipitation Estimates at Fine Scales, Journal of Hydrometeorology, 8, 38 – 55, https://doi.org/10.1175/JHM560.1, 2007.

Kummerow, C., Barnes, W., Kozu, T., Shiue, J., and Simpson, J.: The Tropical Rainfall Measuring Mission (TRMM) Sensor Package, Journal of Atmospheric and Oceanic Technology, 15, 809 – 817, https://doi.org/10.1175/1520-0426(1998)015<0809:TTRMMT>2.0.CO;2, 1998.

625 Li, W., Schumacher, C., and McFarlane, S. A.: Radiative heating of the ISCCP upper level cloud regimes and its impact on the large-scale tropical circulation, Journal of Geophysical Research: Atmospheres, 118, 592–604, https://doi.org/10.1002/jgrd.50114, 2013.

Liao, X., Rossow, W. B., and Rind, D.: Comparison between SAGE II and ISCCP high-level clouds: 2. Locating cloud tops, Journal of Geophysical Research: Atmospheres, 100, 1137–1147, https://doi.org/https://doi.org/10.1029/94JD02430, 1995.

Liu, C.: Geographical and seasonal distribution of tropical tropopause thin clouds and their relation to deep convection and water vapor viewed from satellite measurements, Journal of Geophysical Research: Atmospheres, 112, https://doi.org/https://doi.org/10.1029/2006JD007479, 2007.

Liu, Z., Ostrenga, D., Teng, W., and Kempler, S.: Tropical Rainfall Measuring Mission (TRMM) Precipitation Data and Services for Research and Applications, Bulletin of the American Meteorological Society, 93, 1317 – 1325, https://doi.org/10.1175/BAMS-D-11-00152.1, 2012.

L'Ecuyer, T. S. and Stephens, G. L.: The Tropical Atmospheric Energy Budget from the TRMM Perspective. Part II: Evaluating GCM Representations of the Sensitivity of Regional Energy and Water Cycles to the 1998–99 ENSO Cycle, Journal of Climate, 20, 4548 – 4571, https://doi.org/10.1175/JCLI4207.1, 2007.

Mace, G. G., Zhang, Q., Vaughan, M., Marchand, R., Stephens, G., Trepte, C., and Winker, D.: A description of hydrometeor layer occurrence statistics derived from the first year of merged Cloudsat and CALIPSO data, Journal of Geophysical Research: Atmospheres, 114, https://doi.org/10.1029/2007JD009755, 2009.

Machado, L. A. T., Rossow, W. B., Guedes, R. L., and Walker, A. W.: Life Cycle Variations of Mesoscale Convective Systems over the Americas, Monthly Weather Review, 126, 1630 – 1654, https://doi.org/10.1175/1520-0493(1998)126<1630:LCVOMC>2.0.CO;2, 1998.

Mapes, B. E.: Gregarious tropical convection, Journal of Atmospheric Sciences, 50, 2026–2037, https://doi.org/10.1175/1520-0469(1993)050<2026:GTC>2.0.CO;2, 1993.

Masunaga, H. and Bony, S.: Radiative Invigoration of Tropical Convection by Preceding Cirrus Clouds, Journal of the Atmospheric Sciences, 75, 1327–1342, https://doi.org/10.1175/jas-d-17-0355.1, 2018.

Masunaga, H. and Takahashi, H.: The Energetics of the Lagrangian Evolution of Tropical Convective Systems, Journal of the Atmospheric Sciences, 81, 783 – 799, https://doi.org/10.1175/JAS-D-23-0141.1, 2024.

Moncrieff, M. W.: Organized Convective Systems: Archetypal Dynamical Models, Mass and Momentum Flux Theory, and Parametrization, Quarterly Journal of the Royal Meteorological Society, 118, 819–850, https://doi.org/https://doi.org/10.1002/qj.49711850703, 1992.

Needham, M. R. and Randall, D. A.: Linking Atmospheric Cloud Radiative Effects and Tropical Precipitation, Geophysical Research Letters, 48, e2021GL094 004, https://doi.org/https://doi.org/10.1029/2021GL094004, e2021GL094004 2021GL094004, 2021.

Negri, A. J., Bell, T. L., and Xu, L.: Sampling of the Diurnal Cycle of Precipitation Using TRMM, Journal of Atmospheric and Oceanic Technology, 19, 1333 – 1344, https://doi.org/10.1175/1520-0426(2002)019<1333:SOTDCO>2.0.CO;2, 2002.

Nesbitt, S. W., Zipser, E. J., and Cecil, D. J.: A Census of Precipitation Features in the Tropics Using TRMM: Radar, Ice Scattering, and Lightning Observations, Journal of Climate, 13, 4087 – 4106, https://doi.org/10.1175/1520-0442(2000)013<4087:ACOPFI>2.0.CO;2, 2000.

Protopapadaki, S. E., Stubenrauch, C. J., and Feofilov, A. G.: Upper tropospheric cloud systems derived from IR sounders: properties of cirrus anvils in the tropics, Atmospheric Chemistry and Physics, 17, 3845–3859, https://doi.org/10.5194/acp-17-3845-2017, 2017.

Roca, R. and Fiolleau, T.: Extreme precipitation in the tropics is closely associated with long-lived convective systems, Communications Earth & Environment volume, 1, https://doi.org/10.1038/s43247-020-00015-4, 2020.

Roca, R., Aublanc, J., Chambon, P., Fiolleau, T., and Viltard, N.: Robust observational quantification of the contribution of mesoscale convective systems to rainfall in the tropics, Journal of Climate, 27, 4952–4958, https://doi.org/10.1175/JCLI-D-13-00628.1, 2014.

Schumacher, C., Houze Jr, R. A., and Kraucunas, I.: The tropical dynamical response to latent heating estimates derived from the TRMM precipitation radar, Journal of the Atmospheric Sciences, 61, 1341–1358, https://doi.org/10.1175/1520-0469(2004)061<1341:TTDRTL>2.0.CO;2, 2004.

Shige, S., Takayabu, Y. N., Tao, W.-K., and Johnson, D. E.: Spectral retrieval of latent heating profiles from TRMM PR data. Part I: Development of a model-based algorithm, Journal of applied meteorology, 43, 1095–1113, https://doi.org/10.1175/1520-0450(2004)043<1095:SROLHP>2.0.CO;2, 2004.

Shige, S., Takayabu, Y. N., Tao, W.-K., and Shie, C.-L.: Spectral retrieval of latent heating profiles from TRMM PR data. Part II: Algo-
670   rithm improvement and heating estimates over tropical ocean regions, Journal of applied Meteorology and Climatology, 46, 1098–1124, https://doi.org/10.1175/JAM2510.1, 2007.

Shige, S., Takayabu, Y. N., and Tao, W.-K.: Spectral retrieval of latent heating profiles from TRMM PR data. Part III: Estimating apparent moisture sink profiles over tropical oceans, Journal of applied meteorology and climatology, 47, 620–640, https://doi.org/10.1175/2007JAMC1738.1, 2008.

675   Shige, S., Takayabu, Y. N., Kida, S., Tao, W.-K., Zeng, X., Yokoyama, C., and L'Ecuyer, T.: Spectral Retrieval of Latent Heating Profiles from TRMM PR Data. Part IV: Comparisons of Lookup Tables from Two- and Three-Dimensional Cloud-Resolving Model Simulations, Journal of Climate, 22, 5577 – 5594, https://doi.org/10.1175/2009JCLI2919.1, 2009.

Shige, S., Kida, S., Ashiwake, H., Kubota, T., and Aonashi, K.: Improvement of TMI rain retrievals in mountainous areas, Journal of Applied Meteorology and Climatology, 52, 242–254, https://doi.org/10.1175/JAMC-D-12-074.1, 2013.

680   Stephens, G., Winker, D., Pelon, J., Trepte, C., Vane, D., Yuhas, C., L'ecuyer, T., and Lebsock, M.: CloudSat and CALIPSO within the A-Train: Ten years of actively observing the Earth system, Bulletin of the American Meteorological Society, 99, 569–581, https://doi.org/10.1175/BAMS-D-16-0324.1, 2018.

Stephens, G., Shiro, K., Hakuba, M., Takahashi, H., Pilewskie, J., Andrews, T., Stubenrauch, C., and Wu, L.: Tropical Deep Convection, Cloud Feedbacks and Climate Sensitivity, Surveys in Geophysics, https://doi.org/10.1007/s10712-024-09831-1, 2024.

685   Stubenrauch, C., Chédin, A., Rädel, G., Scott, N., and Serrar, S.: Cloud properties and their seasonal and diurnal variability from TOVS Path-B, Journal of climate, 19, 5531–5553, https://doi.org/10.1175/JCLI3929.1, 2006.

Stubenrauch, C., Kinne, S., and Team, G. C. A.: Assessment of global cloud climatologies, GEWEX News, 19, 6–7, 2009.

Stubenrauch, C., Kinne, S., Mandorli, G., Rossow, W., Winker, D., Ackerman, S., Chepfer, H., Girolamo, L., Garnier, A., Heidinger, A., K.-G, K., Meyer, K., Minnis, P., Platnick, S., Stengel, M., Sun-Mack, S., Veglio, P., Walther, A., Cai, X., and Zhao, G.: Lessons Learned
690   from the Updated GEWEX Cloud Assessment Database, Surveys in Geophysics, pp. 1–50, https://doi.org/10.1007/s10712-024-09824-0, 2024.

Stubenrauch, C. J., Cros, S., Guignard, A., and Lamquin, N.: A 6-year global cloud climatology from the Atmospheric InfraRed Sounder AIRS and a statistical analysis in synergy with CALIPSO and CloudSat, Atmospheric Chemistry and Physics, 10, 7197–7214, https://doi.org/10.5194/acp-10-7197-2010, 2010.

695   Stubenrauch, C. J., Rossow, W. B., Kinne, S., Ackerman, S., Cesana, G., Chepfer, H., Di Girolamo, L., Getzewich, B., Guignard, A., Heidinger, A., et al.: Assessment of global cloud datasets from satellites: Project and database initiated by the GEWEX radiation panel, Bulletin of the American Meteorological Society, 94, 1031–1049, https://doi.org/10.1175/BAMS-D-12-00117.1, 2013.

Stubenrauch, C. J., Feofilov, A. G., Protopapadaki, S. E., and Armante, R.: Cloud climatologies from the infrared sounders AIRS and IASI: strengths and applications, Atmospheric Chemistry and Physics, 17, 13 625–13 644, https://doi.org/10.5194/acp-17-13625-2017, 2017.

700   Stubenrauch, C. J., Caria, G., Protopapadaki, S. E., and Hemmer, F.: 3D radiative heating of tropical upper tropospheric cloud systems derived from synergistic A-Train observations and machine learning, Atmospheric Chemistry and Physics, 21, 1015–1034, https://doi.org/10.5194/acp-21-1015-2021, 2021.

Stubenrauch, C. J., Mandorli, G., and Lemaitre, E.: Convective organization and 3D structure of tropical cloud systems deduced from synergistic A-Train observations and machine learning, Atmospheric Chemistry and Physics, 23, 5867–5884, https://doi.org/10.5194/acp-
705   23-5867-2023, 2023.

Takahashi, H. and Luo, Z. J.: Characterizing tropical overshooting deep convection from joint analysis of CloudSat and geostationary satellite observations, Journal of Geophysical Research: Atmospheres, 119, 112–121, https://doi.org/https://doi.org/10.1002/2013JD020972, 2014.

Takahashi, H., Lebsock, M., Luo, Z. J., Masunaga, H., and Wang, C.: Detection and Tracking of Tropical Convective Storms Based on Globally Gridded Precipitation Measurements: Algorithm and Survey over the Tropics, Journal of Applied Meteorology and Climatology,
710   60, 403 – 421, https://doi.org/10.1175/JAMC-D-20-0171.1, 2021.

Tao, W.-K., Smith, E. A., Adler, R. F., Haddad, Z. S., Hou, A. Y., Iguchi, T., Kakar, R., Krishnamurti, T., Kummerow, C. D., Lang, S., et al.: Retrieval of latent heating from TRMM measurements, Bulletin of the American Meteorological Society, 87, 1555–1572, https://doi.org/10.1175/BAMS-87-11-1555, 2006.

Tao, W.-K., Takayabu, Y. N., Lang, S., Shige, S., Olson, W., Hou, A., Skofronick-Jackson, G., Jiang, X., Zhang, C., Lau, W., et al.: TRMM
715   latent heating retrieval: Applications and comparisons with field campaigns and large-scale analyses, Meteorological Monographs, 56, 2–1, https://doi.org/10.1175/AMSMONOGRAPHS-D-15-0013.1, 2016.

Tao, W.-K., Lang, S., and Iguchi, T.: Latent Heating from TRMM and GPM Measurement, in: IGARSS 2018 - 2018 IEEE International Geoscience and Remote Sensing Symposium, pp. 8343–8346, https://doi.org/10.1109/IGARSS.2018.8517918, 2018.

Tao, W.-K., LangG, S., Iguchi, T., and Song, Y.: Goddard Latent Heating Retrieval Algorithm for TRMM and GPM, Journal of the Meteoro-
720   logical Society of Japan. Ser. II, 100, 293–320, https://doi.org/10.2151/jmsj.2022-015, 2022.

Wylie, D., Jackson, D. L., Menzel, W. P., and Bates, J. J.: Trends in global cloud cover in two decades of HIRS observations, Journal of climate, 18, 3021–3031, https://doi.org/10.1175/JCLI3461.1, 2005.